Concentrated Dual-cation Electrolyte Strategy for Aqueous Zinc-ion Batteries

Yunpei Zhu,†[a] Jun Yin,†[b] Xueli Zheng,†[c] Abdul-Hamid Emwas,[d] Yongjiu Lei,[a] Omar F. Mohammed,[b] Yi Cui,[c,e] Husam N. Alshareef*[a]

[a] *Material Science and Engineering, King Abdullah University of Science and Technology (KAUST), Thuwal 23955-6900, Saudi Arabia. E-mail: husam.alshareef@kaust.edu.sa*

[b] *Advanced Membranes & Porous Materials Center, KAUST Catalysis Center, Division of Physical Science and Engineering King Abdullah University of Science and Technology (KAUST), Thuwal 23955-6900, Saudi Arabia.*

[c] *Department of Materials Science and Engineering, Stanford University, Stanford, California 94305, United States.*

[d] *Core Labs, King Abdullah University of Science and Technology (KAUST), Thuwal 23955-6900, Saudi Arabia.*

[e] *Stanford Institute for Materials and Energy Sciences, SLAC National Accelerator Laboratory, Menlo Park, California 94025, United States.*

† These authors contributed equally to this work.

1. Experimental Details.

1.1. Materials Synthesis.

Synthesis of $Na_2V_6O_{16}\cdot nH_2O$ (NVO) nanofibers. Typically, 90 g of commercial V_2O_5 powders were slowly dispersed in 100 ml of 3M NaCl aqueous solution. After vigorously stirring for three days at room temperature, the dark brown hydrogel was washed with distilled water, collected by centrifugation, and dried in a vacuum oven overnight. During the synthesis process, the suspension gradually changed from orange to dark orange, brown, and dark brown, together with the gradual change of the pH from nearly neutral to highly acidic. These two changes indicated the successful dissolution of V_2O_5 and the simultaneous formation of new phase, which was along with H_2O and Na^+ cointercalation to ensure the charge balance of the overall reaction system.

Synthesis of $K_2V_6O_{16}\cdot nH_2O$ (KVO) nanofibers. The whole process is similar to the synthesis of NVO nanofiber except for using 9 g of commercial V_2O_5 powders and 10 ml of 3M KCl. The color of the final KVO product is dark red.

1.2. Materials Characterizations.

Scanning electron microscopy (SEM) and transmission electron microscopy (TEM) images were recorded on an FEI Teneo at a high vacuum with an accelerating voltage of 5 kV and FEI Titan Cs Probe electron microscope equipped with image-corrector operated at 300 kV, respectively. X-ray diffraction (XRD) patterns were recorded on a Bruker D8 Advance powder diffractometer at 40 kV and 40 mA using Co-Kα radiation. Attenuated total reflectance (ATR) Fourier-transform infrared (FT-IR) spectra were recorded on a Nicolet 6700 spectrometer. All liquid-state NMR spectra were recorded using a Bruker 600 MHz AVANACIII NMR spectrometer equipped with BBO probe (BrukerBioSpin, Rheinstetten, Germany). All solid-state NMR spectra were acquired using a Bruker 400 MHz AVANACIII NMR spectrometer equipped with 4 mm Bruker double-resonance MAS probe (BrukerBioSpin, Rheinstetten, Germany). Raman spectrum was recorded on a micro-Raman spectrometer (LabRAM ARAMIS, Horiba-Jobin Yvon) with notch filters cutting at 100 cm^{-1} with the use of a laser wavelength of 532 nm. Ionic conductivity was performed on an Oaktont CON 6^+ conductivity meter at room temperature. Prior to each measurement, the calibration was conducted in in 12 880 mS cm^{-1} calibration solution (HI7030L by Hanna Instruments). Viscosity measurements were recorded on an oscillatory rheometer (ARES-G2, TA Instruments) at room temperature. 1 mL of the solution was added to a sample cup, and the sample was analyzed in a cone and cup geometry. X-ray photoelectron spectra (XPS) were collected with the use of a Thermo Escalab 250 spectrometer equipped with an Al-Kα X-ray source (1486.6 eV). V *L*-edge X-ray absorption was performed at beamline 10-1 at the Stanford Synchrotron Radiation Lightsource (SSRL). Bulk sensitive absorption spectra were recorded using total fluorescence yield. V *K*-edge X-ray absorption was performed at beamline 4-1 at SSRL. The collected data were further calibrated and normalized by Athena software.

1.3. Electrochemical Measurements.

A slurry was first made using 70% NVO, 20% conductive carbon black, and 10% polyvinylidene difluoride (PVDF) binder. The homogeneous slurry was then cast onto a Ti foil using a doctor blading method, followed by drying in a vacuum oven at 60 °C. The mass loading of active materials was 3–4 mg cm^{-2}. The electrolyte was the solution of 0.5m $Zn(ClO_4)_2$ with 18m $NaClO_4$, and Zn metal foil was used as the anode. CR2032 coin cells were assembled by stacking the cathode and anode separated by glass fiber. Galvanostatic charge-discharge testing (GCD) and long-term stability testing were conducted on NEWARE multichannel workstation (CT-4800-5V10mA, China). Cyclic voltammetry (CV) was recorded using VMP3 Biologic potentiostat (Biologic, France).

1.4. Calculation Methods.

The *ab-initio* MD simulations were carried out using the projector-augmented wave (PAW) method as implemented in the VASP code.[S1,S2] The generalized gradient approximation (GGA) with the Perdew-Burke-Ernzerhof (PBE) exchange-correlation functional was used. The electrolyte structures were built based on the aqueous electrolytes with 1 m $Zn(ClO_4)_2$ and two different concentrations of $NaClO_4$ (18 m and 36 m). The simulation cells with the dimension of 14.8 × 14.8 × 14.8 Å contained 1 $Zn(ClO_4)_2$ and 110 water for 0.5m $Zn(ClO_4)_2$, 1 $Zn(ClO_4)_2$, 18 $NaClO_4$ and 110 water for the 0.5m $Zn(ClO_4)_2$ + 9m $NaClO_4$ electrolyte, and 1 $Zn(ClO_4)_2$, 36 $NaClO_4$ and 110 water for the 0.5m $Zn(ClO_4)_2$ + 18m $NaClO_4$ electrolyte. The atomic positions of all the initial structures were fully relaxed until the supercells had forces on each atom less than 0.01 eV/Å. The plane-wave basis set cutoffs of the wavefunctions were set at 450 eV. After the structural optimizations, the MD simulations were performed with a time step of 1 fs, and the NVT ensemble was used to control the temperatures (300 K, 350 K, and 400 K). After 5000 fs equilibration run, another 3000 fs production run was performed for the analysis.

The adsorption energies (E_{ads}) between H_2O molecule/Zn^{2+} ion and Zn/$ZnCl_2$ were calculated with the equation of $E_{ads} = E(\text{total}) - E(\text{Zn/ZnCl}_2) - E(\text{H}_2\text{O/Zn}^{2+})$, where E(total) is the total energy of the interface after H_2O/Zn^{2+} adsorption, and $E(\text{Zn/ZnCl}_2)$ and $E(\text{H}_2\text{O/Zn}^{2+})$ represent the energy of the individual parts. The Zn^{2+}-coordinated clusters obtained from MD runs (*i.e.*, $Zn^{2+}\cdot 6H_2O$, $Zn^{2+}\cdot 3ClO_4^{-}\cdot 3H_2O$, and $Zn^{2+}\cdot 4ClO_4^{-}\cdot 2H_2O$) were further optimized at GGA/PBE level, and the corresponding dissociation energies (E_{dis}) were calculated with the equation of $E_{dis} = E(\text{total}) - E(\text{Zn}^{2+}) - E(n\text{H}_2\text{O}\cdot 6\text{-}n\text{ClO}_4^{-})$, where n = 6, 3, or 2, E(total) is the total energy of the cluster, and $E(\text{Zn}^{2+})$ is the energy of Zn^{2+} ion, and $E(n\text{H}_2\text{O}\cdot 6\text{-}n\text{ClO}_4^{-})$ is the total energy of H_2O and ClO_4^{-}.

2. Supplementary Fig.s.

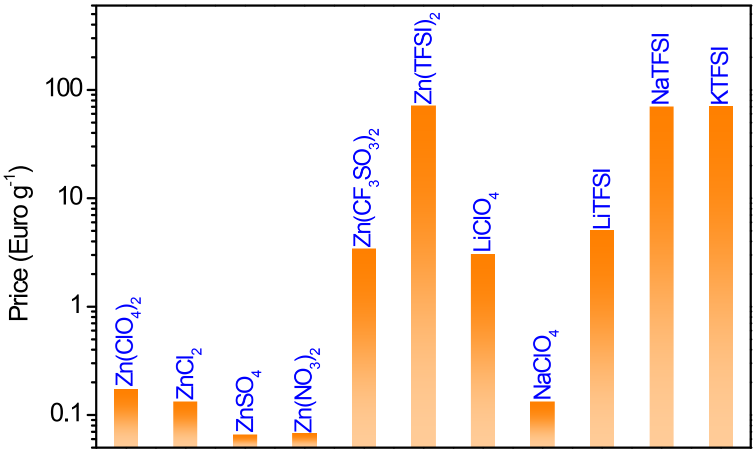

Fig. S1 Price comparison of the commonly used salts in different batteries (OTf: triflate, TFSI: bis(trifluoromethane)sulfonimide). The price is calculated based on the available largest pack size from Sigma. $Zn(ClO_4)_2$ and $NaClO_4$ are 30–40 times cheaper than the conventional LiTFSI. Since water is nearly free, our HCZE (0.5m $Zn(ClO_4)_2$ + $NaClO_4$) shows a price of 0.17 Euro g^{-1}, much cheaper than the conventional Li-ion electrolyte of 1M LiTFSI dissolved in EC/DMC (*v*:*v* = 3:7) (~1.74 Euro g^{-1}) (EC: ethylene carbonate, DMC: dimethyl carbonate) and even comparable to the price of standard Zn-ion electrolyte of 2M $Zn(CF_3SO_3)_2$ (~0.18 Euro g^{-1}). This highlights the price advantage of our HCZE electrolyte for potential large-scale applications.

Additionally, compared to the frequently used TFSI-based salts in WIS electrolytes, $NaClO_4$ shows the advantage of safety. For example, $NaClO_4$ has been widely used for hybridization reactions in molecular biology, standard DNA extraction, and medicines.[S3] The above discussions highlight the price and safety superiorities of our electrolytes developed in this work.

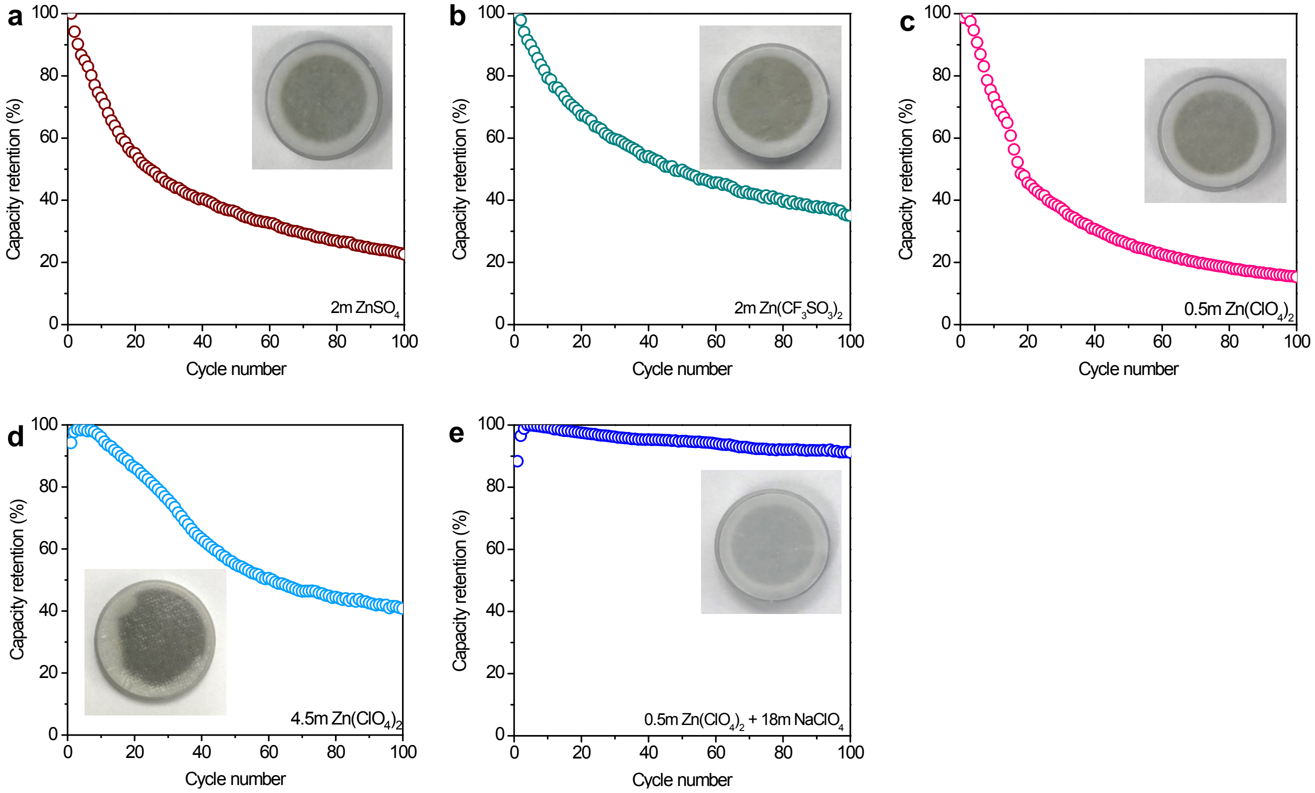

Fig. S2 Stability tests of our NVO cathode in different electrolytes: (a) 2m $ZnSO_4$, (b) 2m $Zn(CF_3SO_3)_2$, (c) 0.5m $Zn(ClO_4)_2$, (d) 4.5m $Zn(ClO_4)_2$, and 0.5m $Zn(ClO_4)_2$ + 18m $NaClO_4$ (*i.e.*, HCZE). The insets show the photos of the batteries after adding 80ul electrolytes. The instant color changes of NVO in low-concentration electrolytes (Fig. S2a-c) and even the concentrated electrolyte of 4.5m $Zn(ClO_4)_2$ indicate the serious dissolution issues because of the existence of a significant amount of “free” water molecules. However, these issues could be significantly prohibited in the most concentrated electrolyte (Fig. S2e).

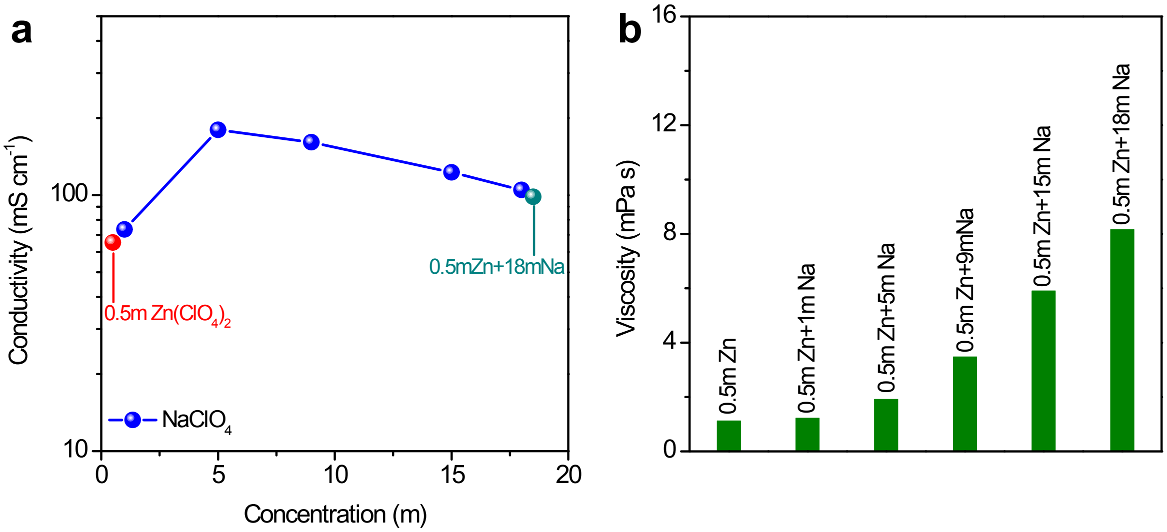

Fig. S3 Plots of ionic conductivity (a) and viscosity (b) of different electrolytes.

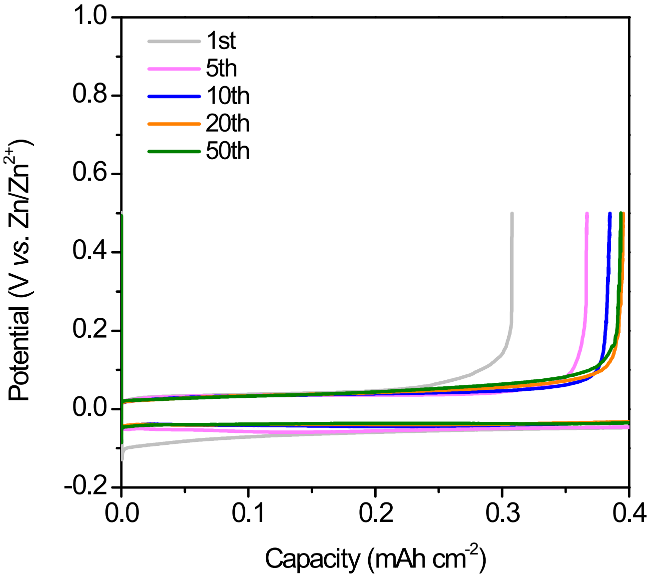

Fig. S4 Capacity-voltage profiles of Ti/Zn cell in HCZE at 0.4 mA cm^{-2}.

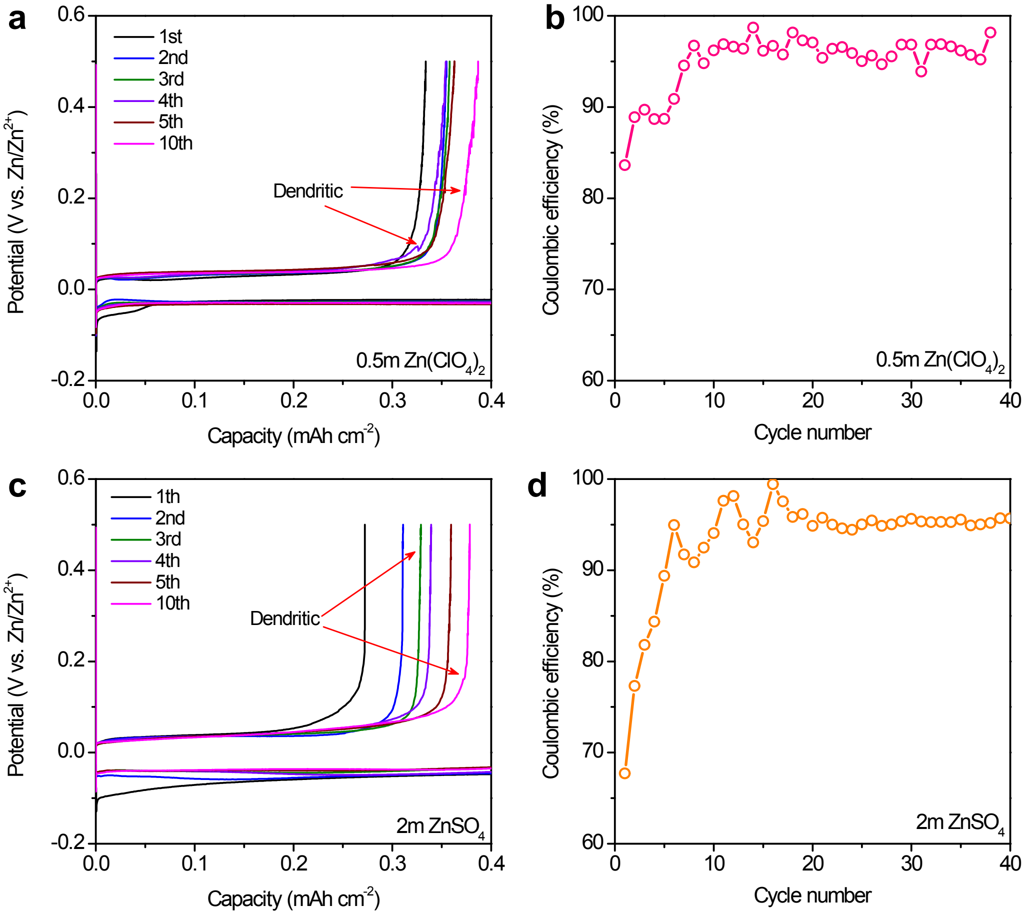

Fig. S5 Capacity-voltage curves of Ti/Zn cells in low-concentration electrolytes of 0.5m $Zn(ClO_4)_2$ (a), 2m $ZnSO_4$ (c), and the corresponding plots of Coulombic efficiency *vs.* cycle number. Dendrite formation and low Coulombic efficiency could be observed in low-concentration electrolytes, which should be due to the parasitic reactions.

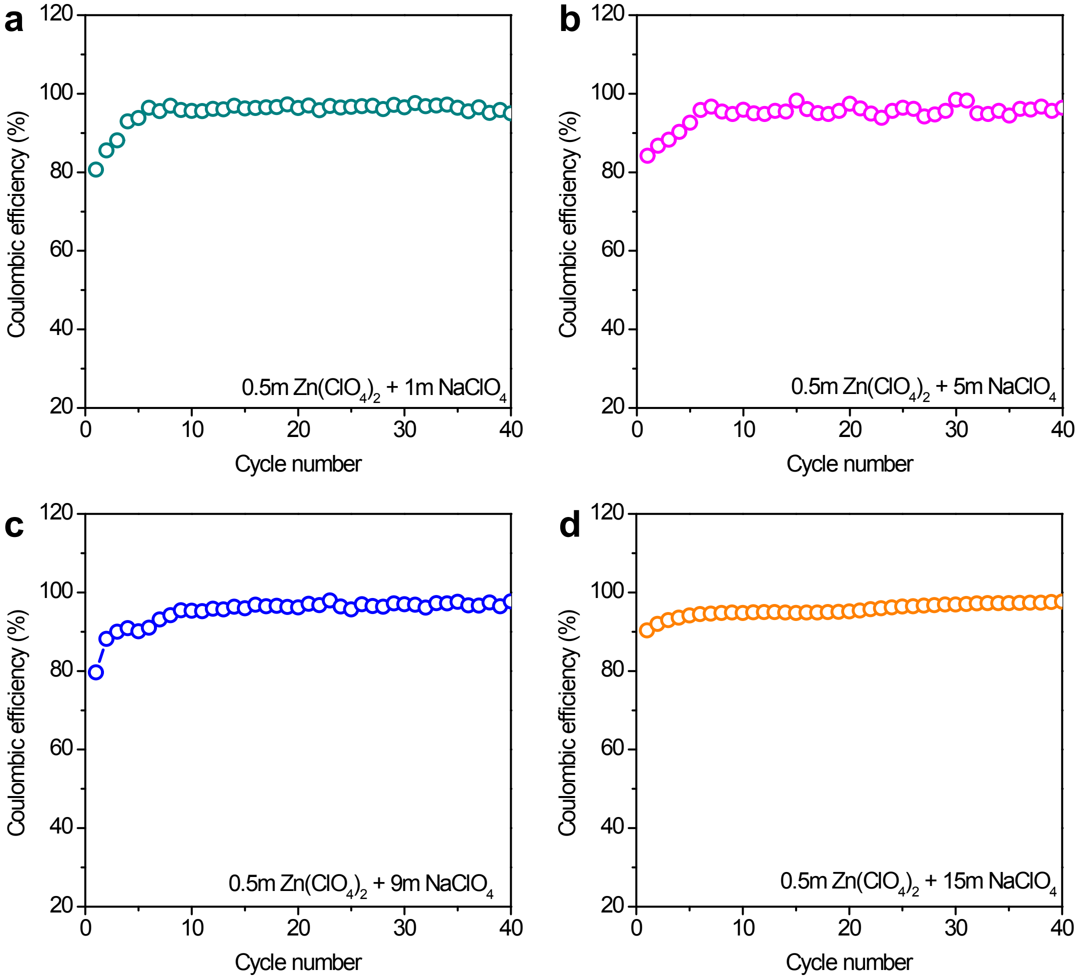

Fig. S6 Plots of Coulombic efficiency of Zn plating/striping on the Ti working electrode in different electrolytes at 1 mA cm^{-2}.

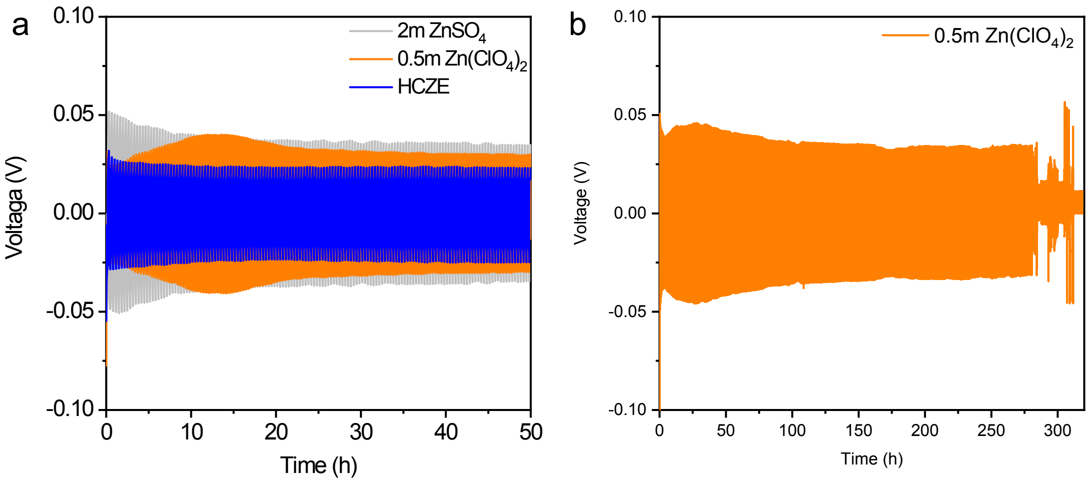

Fig. S7 Zn plating/stripping in Zn/Zn symmetric cells using different electrolytes at 0.2 mA cm^{-2}. The lowest polarization in HCZE indicates the improved Zn plating/stripping kinetics. As shown in Fig. S7b, the Zn/Zn symmetric cell experiences a fast short circuit at a low current density of 0.2 mA cm^{-2} in 0.5m Zn(ClO$_4$)$_2$.

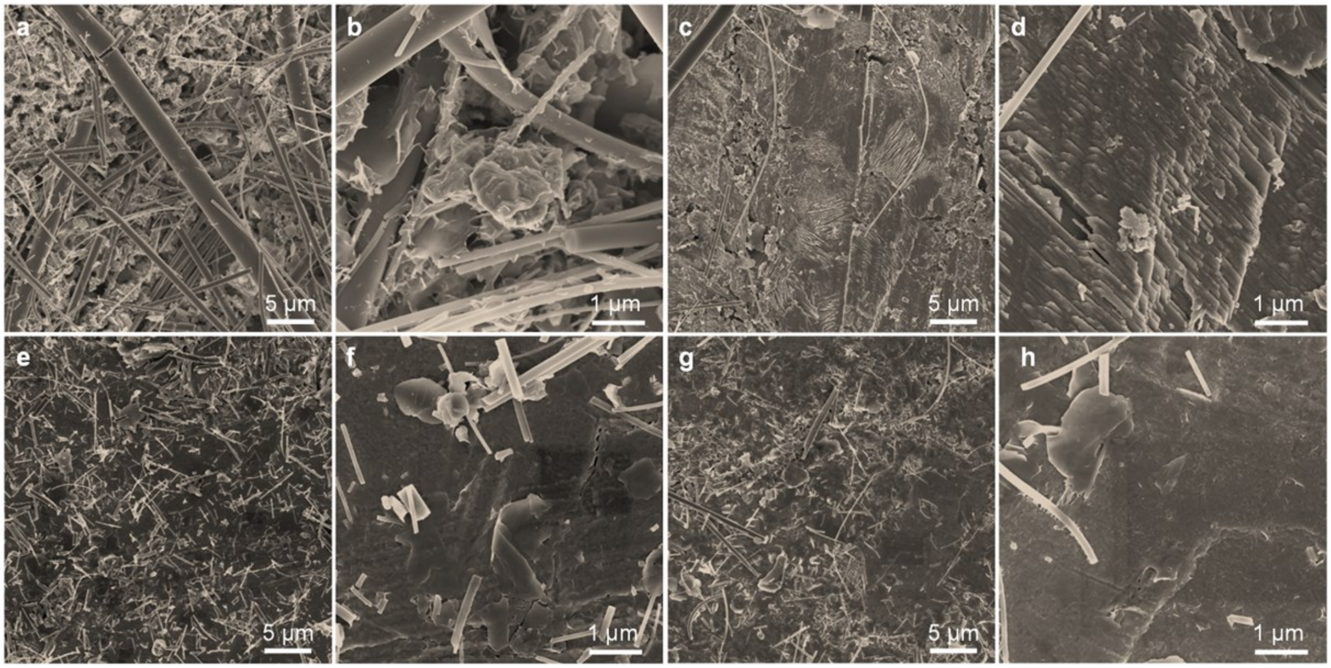

Fig. S8 *Ex-situ* SEM images of Zn anode at selected cycles. (a,b) 0.5m Zn(ClO$_4$)$_2$ after 20 cycles, (c,d) HCZE after 1 cycle, (e,f) HCZE after 20 cycles, and (g,h) HCZE after 50 cycles.

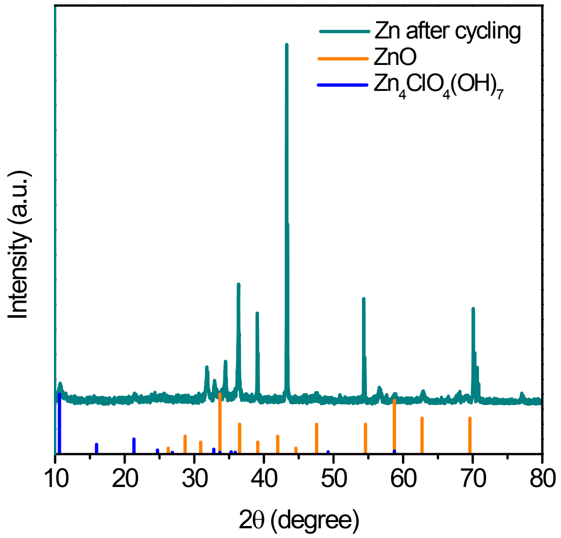

Fig. S9 XRD pattern of the Zn metal anode after 20 cycles in 0.5m $Zn(ClO_4)_2$, showing serious parasitic reactions like corrosion (ZnO) and hydrogen evolution ($Zn_4ClO_4(OH)_7$).

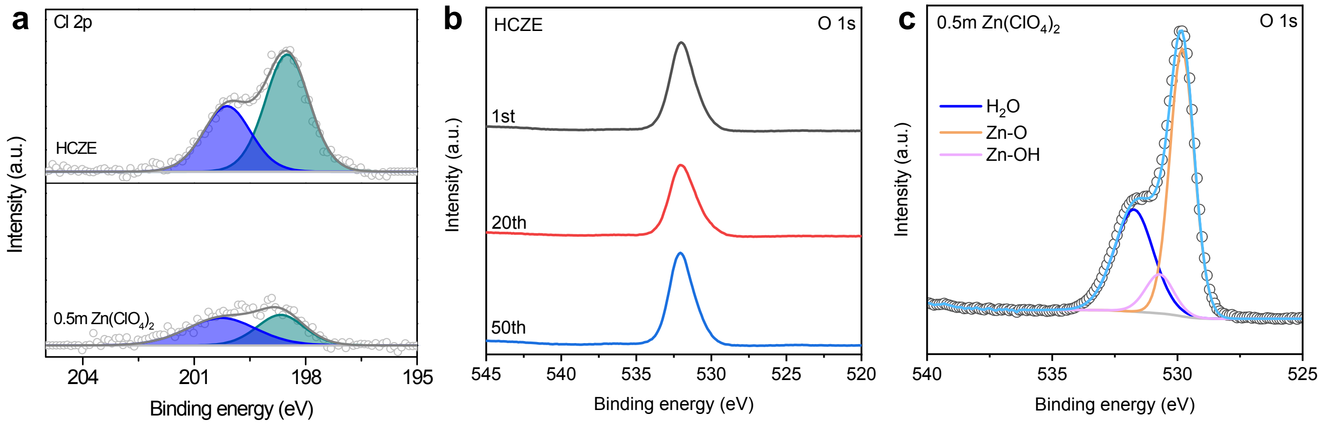

Fig. S10 *Ex-situ* XPS spectra of Zn metal anode using two different electrolytes: Cl 2p core level (a) and O 1s core level (b,c). HCZE delivers one single symmetric peak attributed to adsorbed oxygen species (H_2O). In contrast, Zn metal cycled in 0.5m $Zn(ClO_4)_2$ shows three oxygen species: adsorbed O (H_2O), Zn–O (ZnO), and Zn–OH ($Zn_4ClO_4(OH)_7$). This is consistent with the *ex-situ* XRD analysis, further confirming the occurrence of severe parasitic reactions in the low-concentration electrolyte of 0.5m $Zn(ClO_4)_2$.

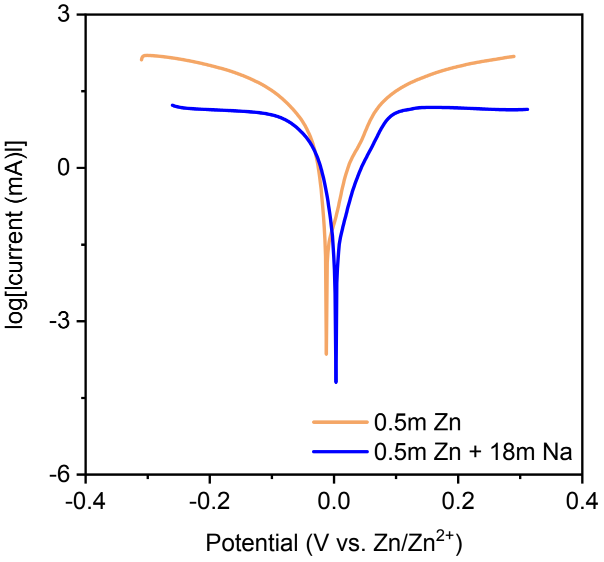

Fig. S11 Linear polarization curves showing the corrosion on Zn using 0.5m $Zn(ClO_4)_2$ and 0.5m $Zn(ClO_4)_2$ + 18m $NaClO_4$ (HCZE). The decreased corrosion current and increased corrosion potential in HCZE indicate the efficient suppression of parasitic reactions (*e.g.*, hydrogen evolution). This is beneficial for the formation of a high-quality $ZnCl_2$ protection layer to enable stable Zn plating/stripping with high Coulombic efficiency.

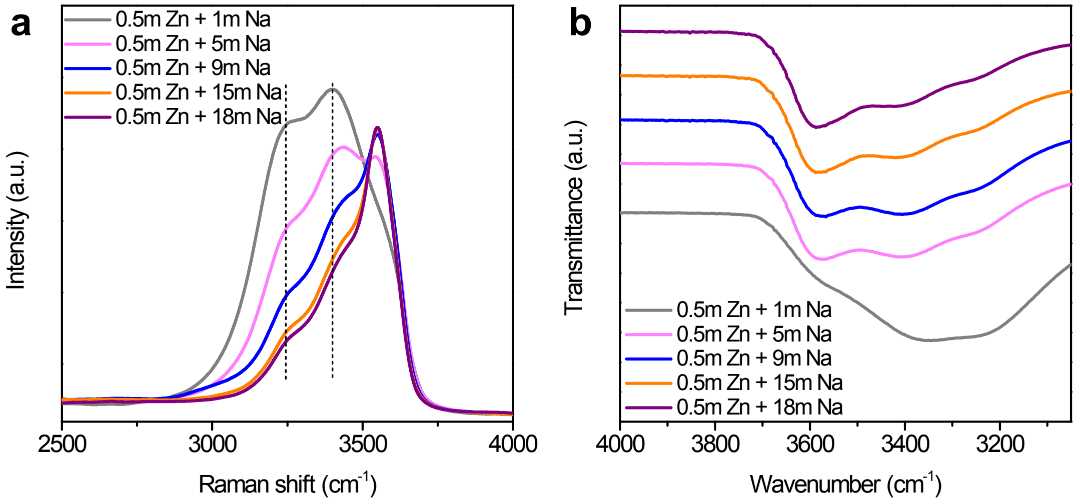

Fig. S12 Raman (a) and ATR-FTIR (b) spectra of the electrolytes with different salt concentrations.

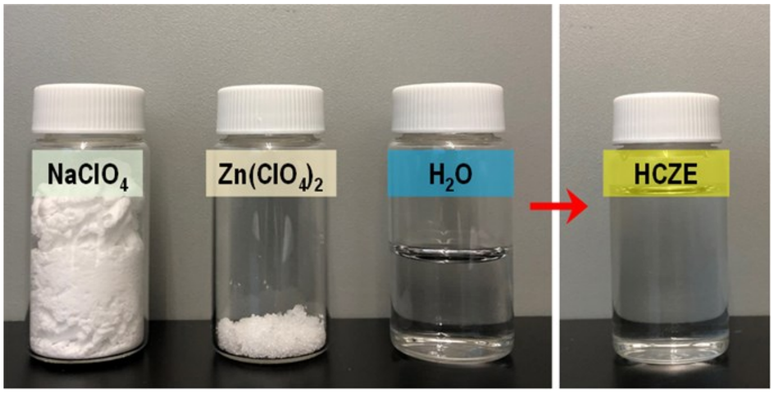

Fig. S13 Stoichiometric amounts of $NaClO_4$, $Zn(ClO_4)_2$, and water were used to prepare the most concentrated electrolyte of HCZE.

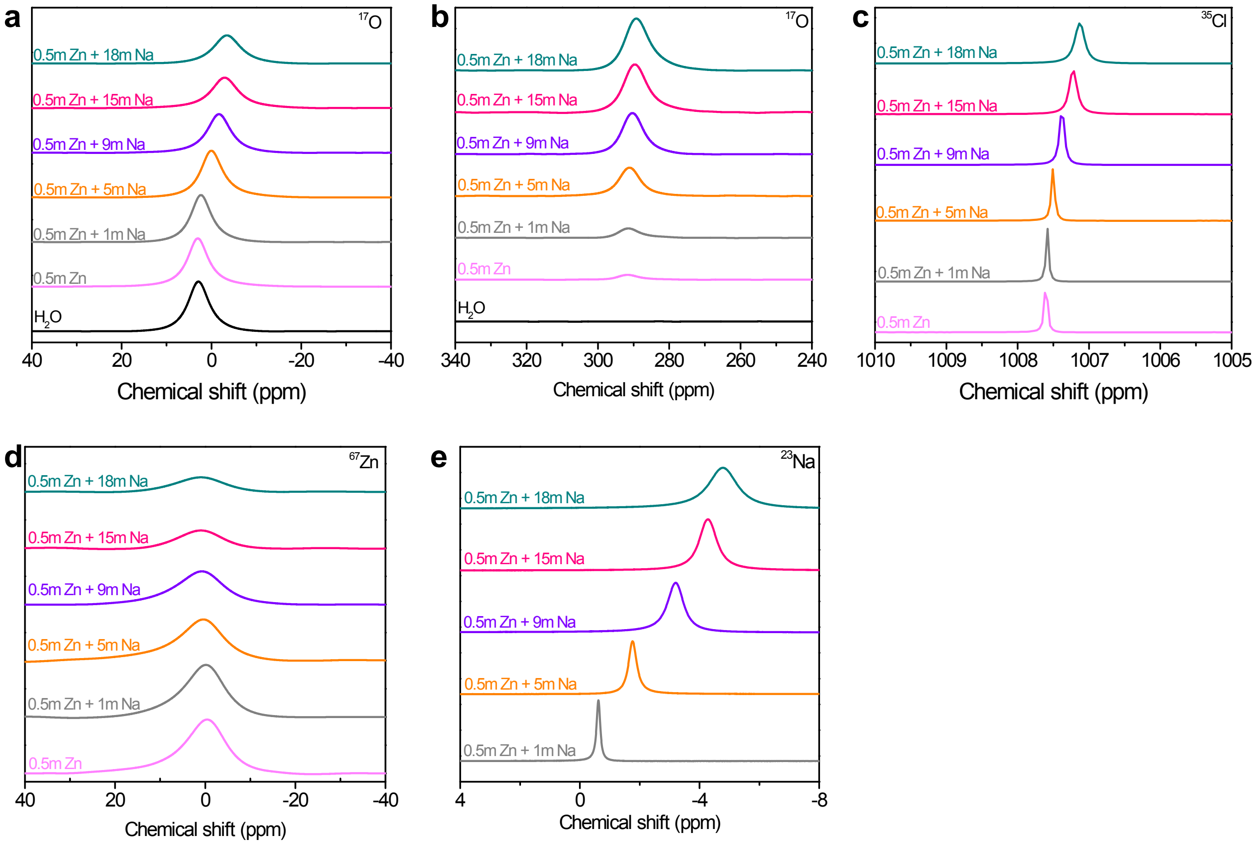

Fig. S14 NMR spectra of the chemical components in the electrolytes with different concentrations. (a) ^{17}O of H_2O, (b) ^{17}O of ClO_4^-, (c) ^{35}Cl of ClO_4^-, (d) ^{67}Zn, and (e) ^{23}Na.

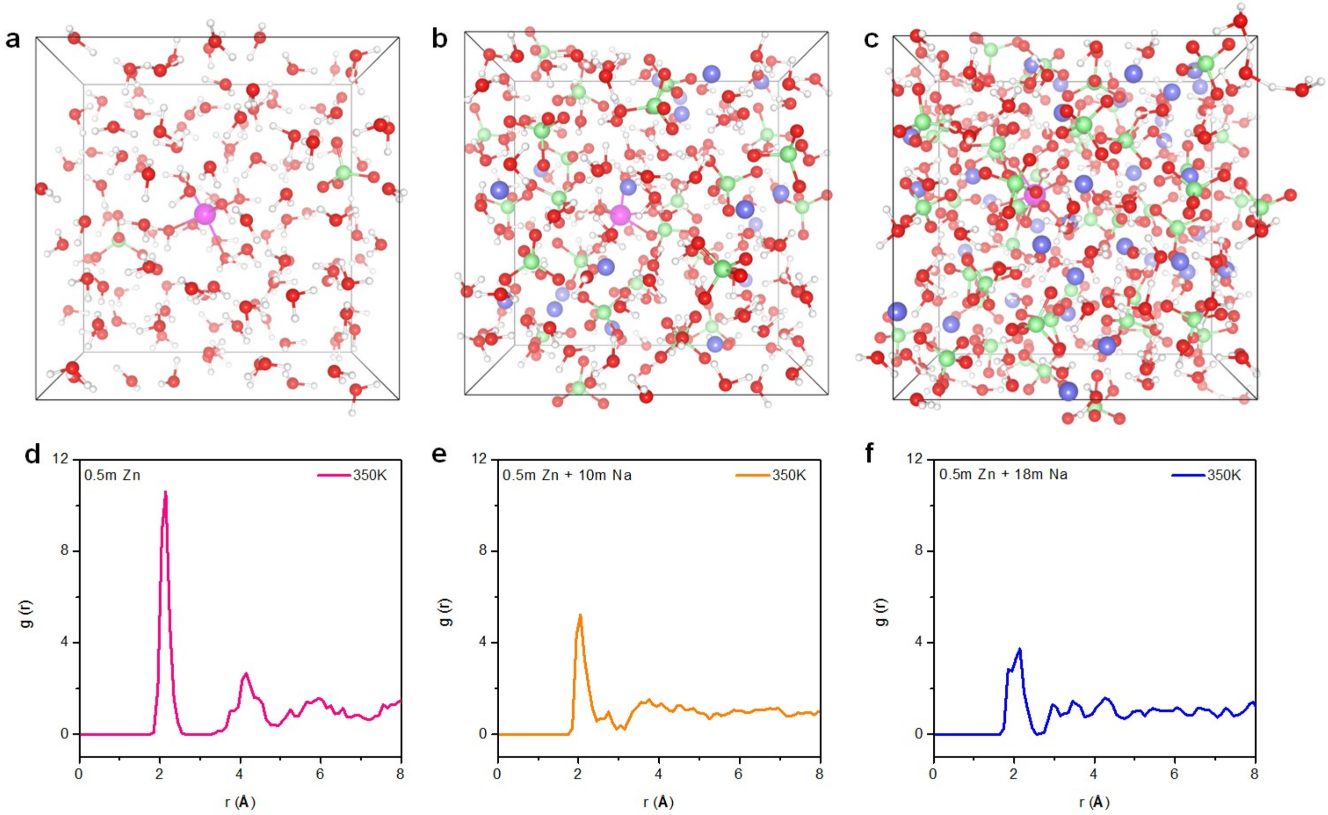

Fig. S15 Snapshots of equilibrium trajectories obtained from *ab-initio* MD simulations at 350 K: (a) 0.5m $Zn(ClO_4)_2$, (b) 0.5m $Zn(ClO_4)_2$ + 9m $NaClO_4$, and (c) 0.5m $Zn(ClO_4)_2$ + 18m $NaClO_4$. (d-f) The corresponding RDFs plots at different concentrations.

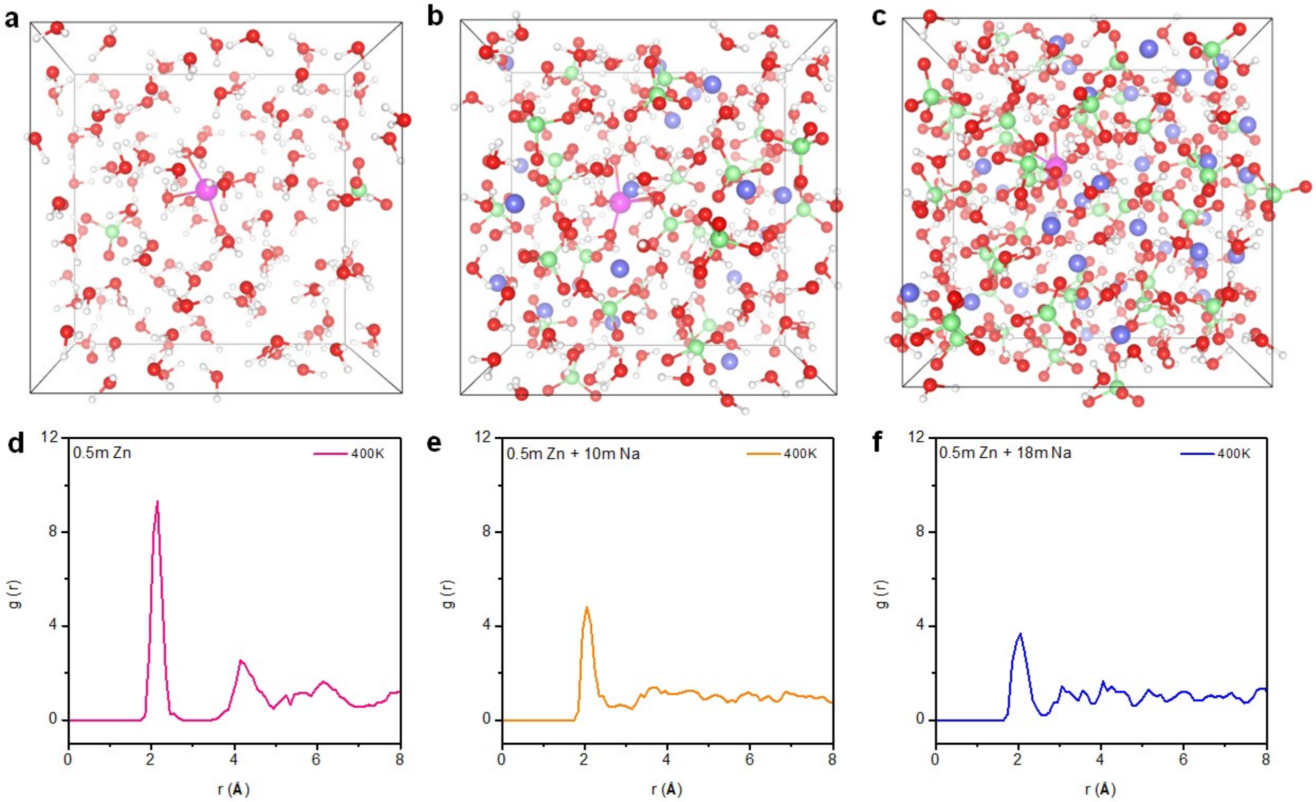

Fig. S16 Snapshots of equilibrium trajectories obtained from *ab-initio* MD simulations at 400 K: (a) 0.5m $Zn(ClO_4)_2$, (b) 0.5m $Zn(ClO_4)_2$ + 9m $NaClO_4$, and (c) 0.5m $Zn(ClO_4)_2$ + 18m $NaClO_4$. (d-f) The corresponding RDFs plots at different concentrations.

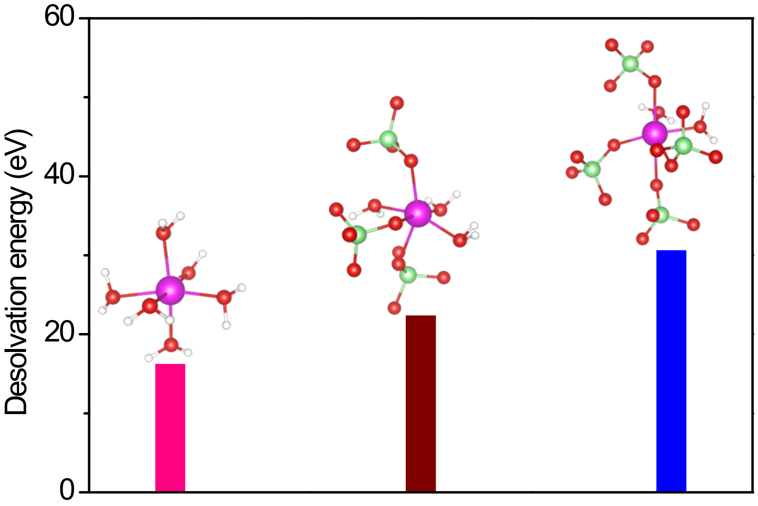

Fig. S17 Comparison of complete dissociation energy of Zn^{2+} in the electrolytes of 0.5m $Zn(ClO_4)_2$, 0.5m $Zn(ClO_4)_2$ + 9m $NaClO_4$, and 0.5m $Zn(ClO_4)_2$ + 18m $NaClO_4$.

Fig. S18 Optical photos of the NVO hydrogel before washing and drying.

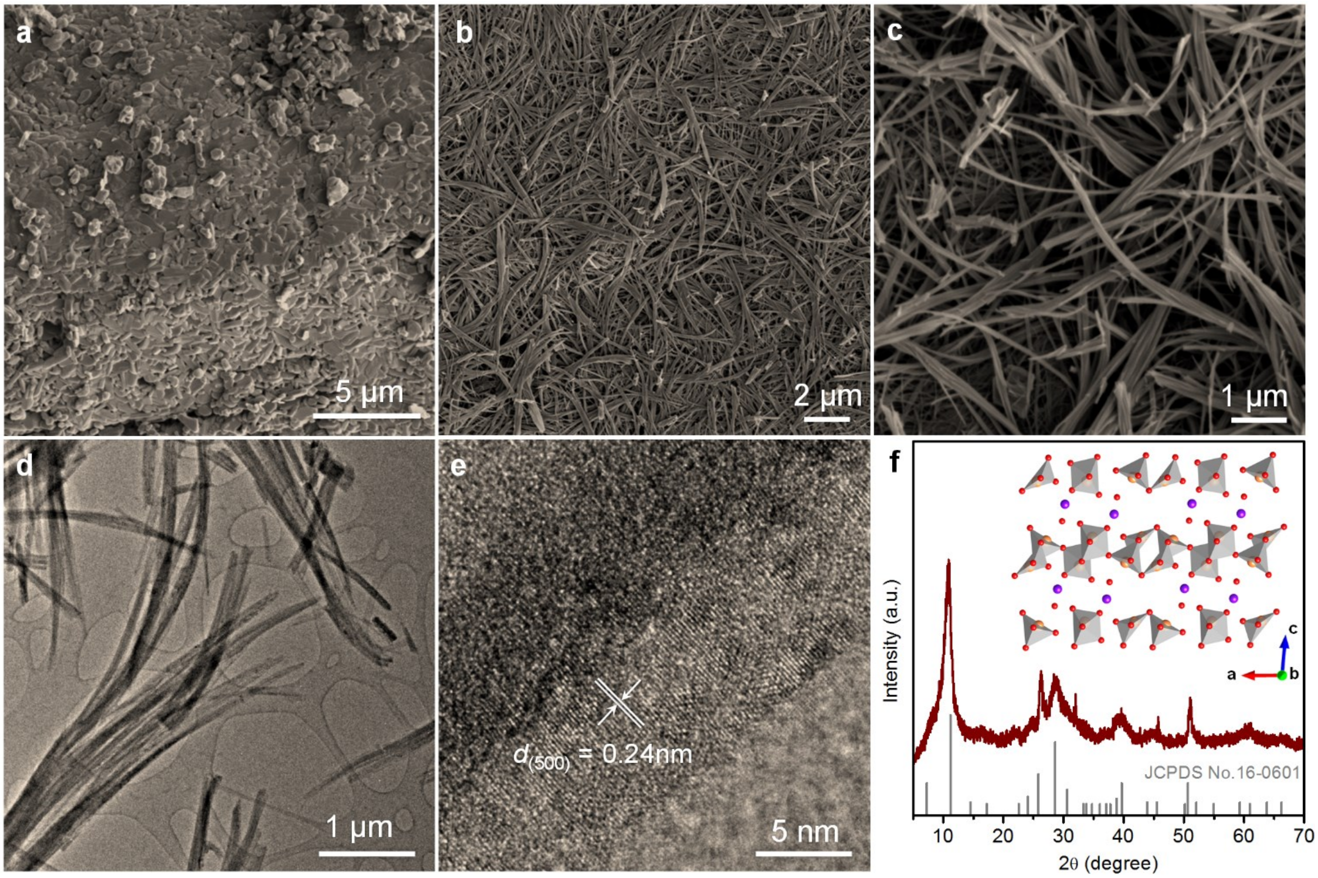

Fig. S19 Characterizations of the synthesized NVO. (a) SEM image of the commercial V_2O_5 nanoparticles. (b,c) SEM and (d,e) TEM images of the NVO nanofibers. High-resolution TEM image of an individual nanofiber shows a lattice spacing of 0.24 nm, corresponding to the *d* spacing of (500) plane of monoclinic $Na_2V_6O_{16}\cdot nH_2O$. This is consistent with the X-ray diffraction (XRD) pattern of the as-synthesized NVO (Fig. S16f), showing a space group of *P*2/*m*. The monoclinic structure of NVO is constructed by the V_3O_8 layers featuring two different zigzag chains (chains of edge-sharing V_2O_8 square pyramids and chains of distorted VO_6 octahedra) (inset of Fig. S16f), while hydrated Na ions are located among the layers.

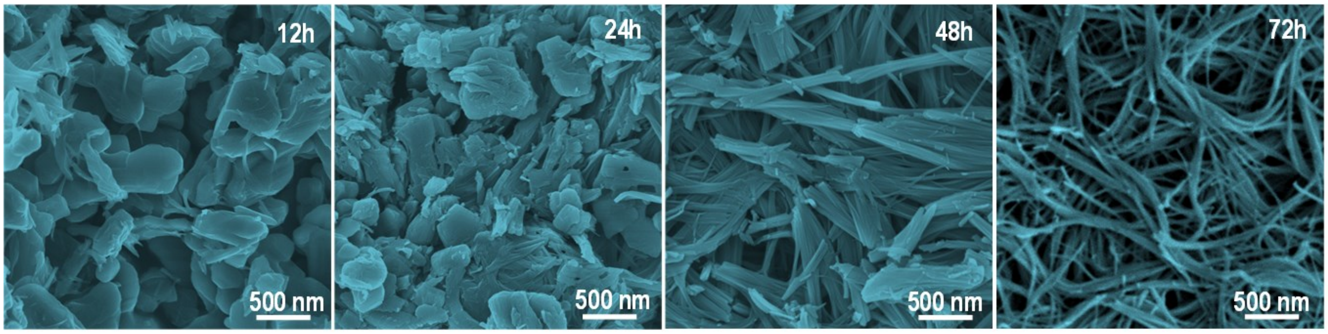

Fig. S20 Time-dependent SEM images of the solid reaction intermediates after mixing V_2O_5 with 3M NaCl.

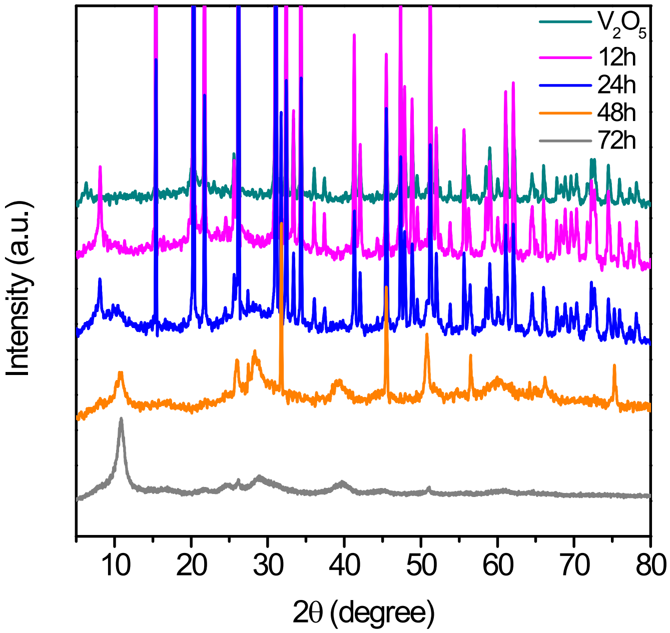

Fig. S21 Time-dependent XRD patterns of the solid reaction intermediates after mixing V_2O_5 with 3M NaCl, showing the gradual disappearance of diffractions from orthorhombic V_2O_5 and the appearance of monoclinic $Na_2V_6O_{16}\cdot nH_2O$.

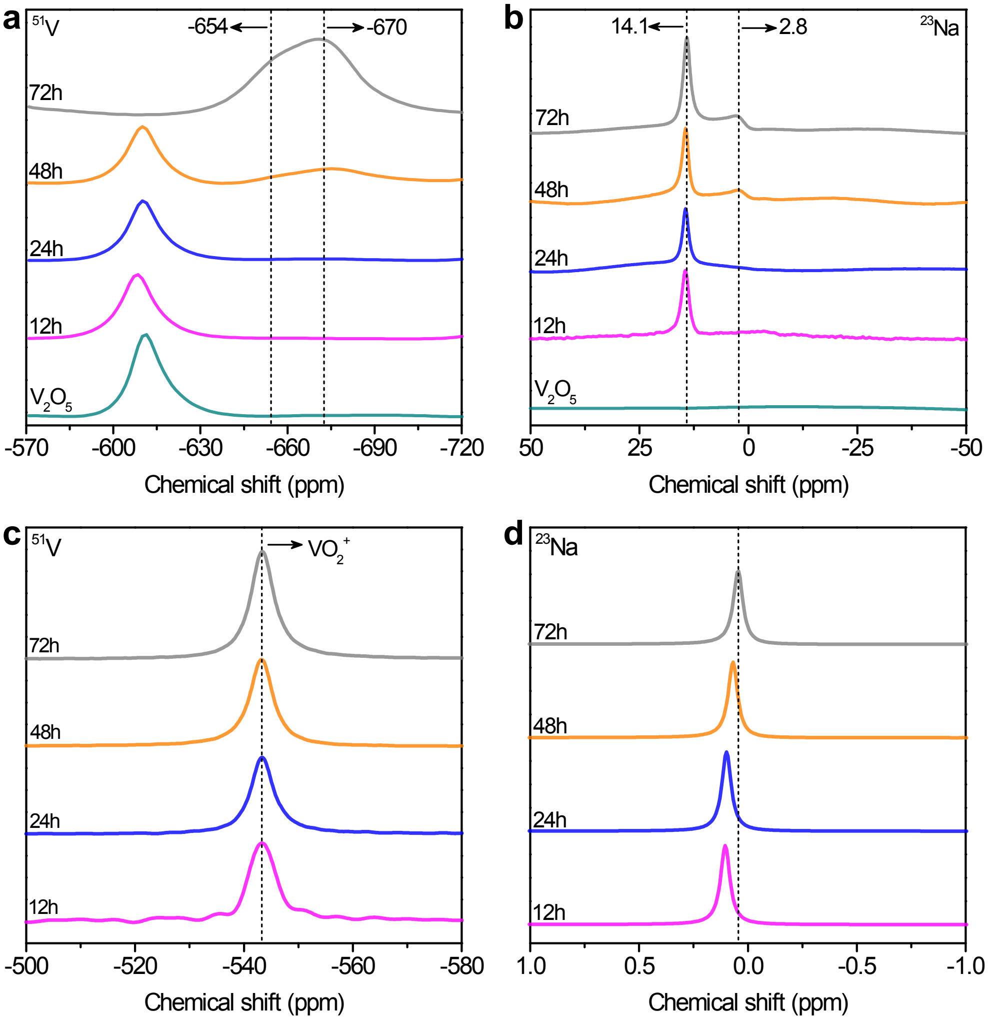

Fig. S22 NMR spectra of the reaction intermediates during the preparation of NVO after mixing V_2O_5 with 3M NaCl. (a) ^{51}V and (b) ^{23}Na NMR spectra of the solid intermediates. (c) ^{51}V and d) ^{23}Na NMR spectra of the liquid intermediates.

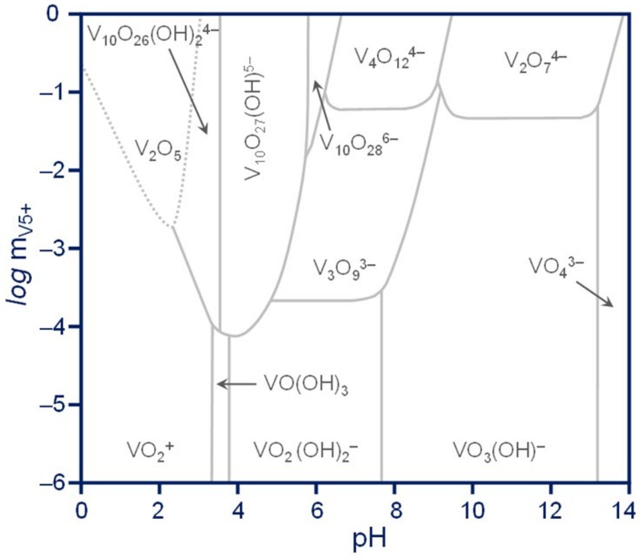

Fig. S23 Vanadium species in aqueous solution depending on the pH conditions and concentrations.

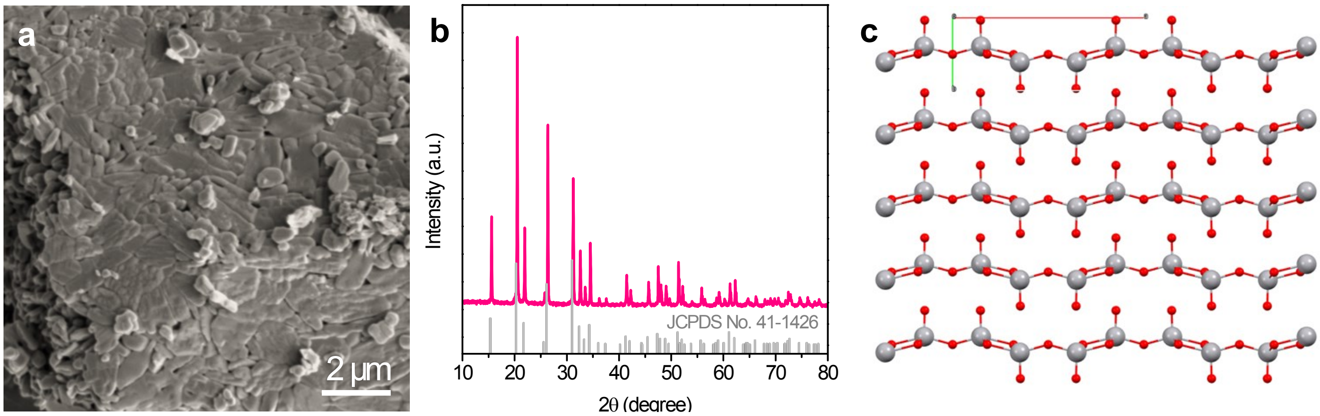

Fig. S24 SEM image (a), XRD pattern (b), and crystalline structure (c) of V_2O_5 after stirring in H_2O for three days, showing the absence of changes in morphology and phase.

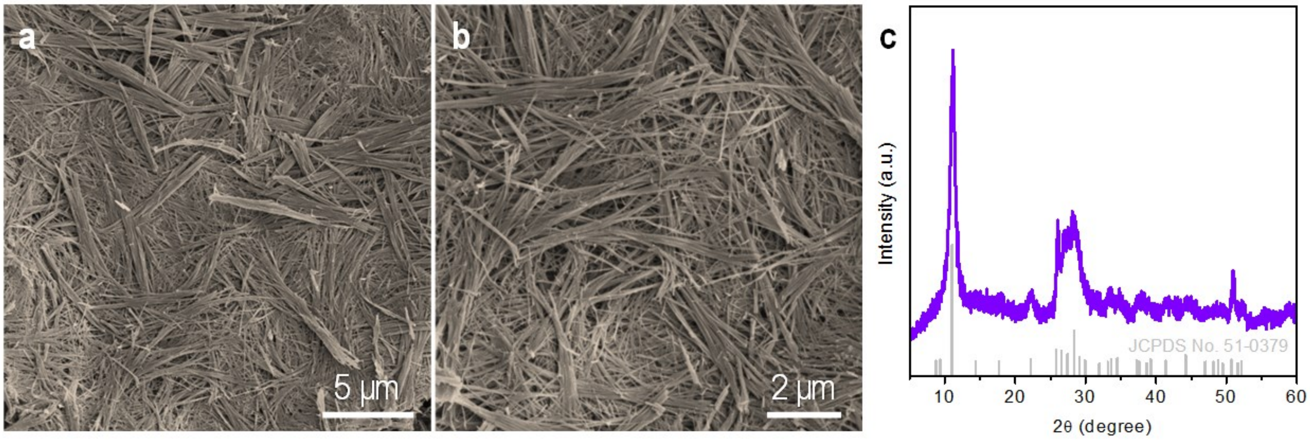

Fig. S25 (a,b) SEM images and (c) XRD pattern of the monoclinic $K_2V_6O_{16}\cdot nH_2O$ nanofibers synthesized through the dissolution-recrystallization strategy.

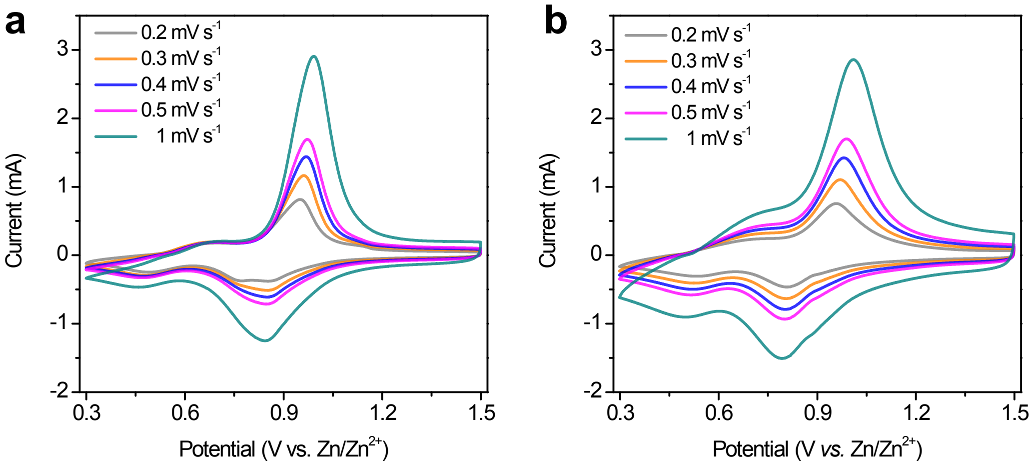

Fig. S26 Sweep voltammetry curves of the NVO cathode in 0.5m $Zn(ClO_4)_2$ (a) and HCZE (b).

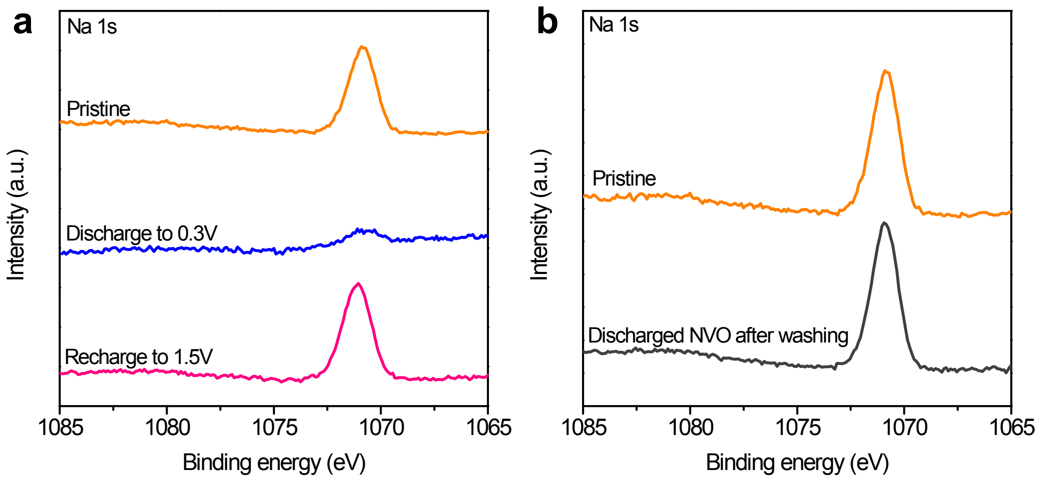

Fig. S27 *Ex-situ* Na 1s core level of the NVO cathode in HCZE. The formation of $Zn_4ClO_4(OH)_7$ nanosheets on the cathode surface weakens the Na 1s signal upon discharge (Fig. S27a). However, after washing the discharged NVO with a large amount of distilled water, the Na 1s signal nearly returns to the pristine state (Fig. S27b), signifying the absence of Na^+ intercalation upon discharge.

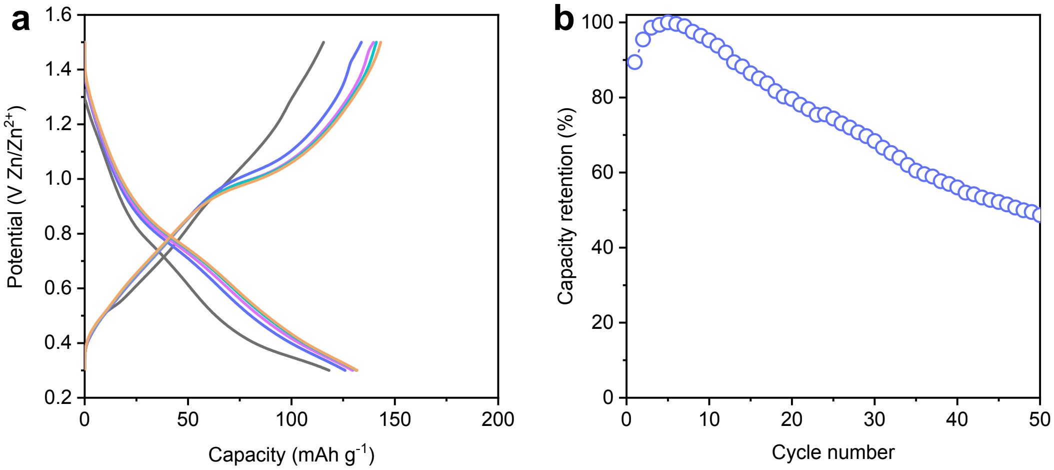

Fig. S28 Galvanostatic charge-discharge curves of the NVO electrode using 18m $NaClO_4$ as the electrolyte (current density: 0.1 A g^{-1}). Compared to the performance of the NVO electrode in HCZE, the much lower capability and insufficient cycling stability in 18m $NaClO_4$ would be related to the larger size of Na^+ (1.02 Å) than Zn^{2+} (0.74 Å) and H^+ (0.87 × 10^{-5} Å. This is similar to the previously reported battery chemistries involving dual-solute electrolytes.[S4-S6]

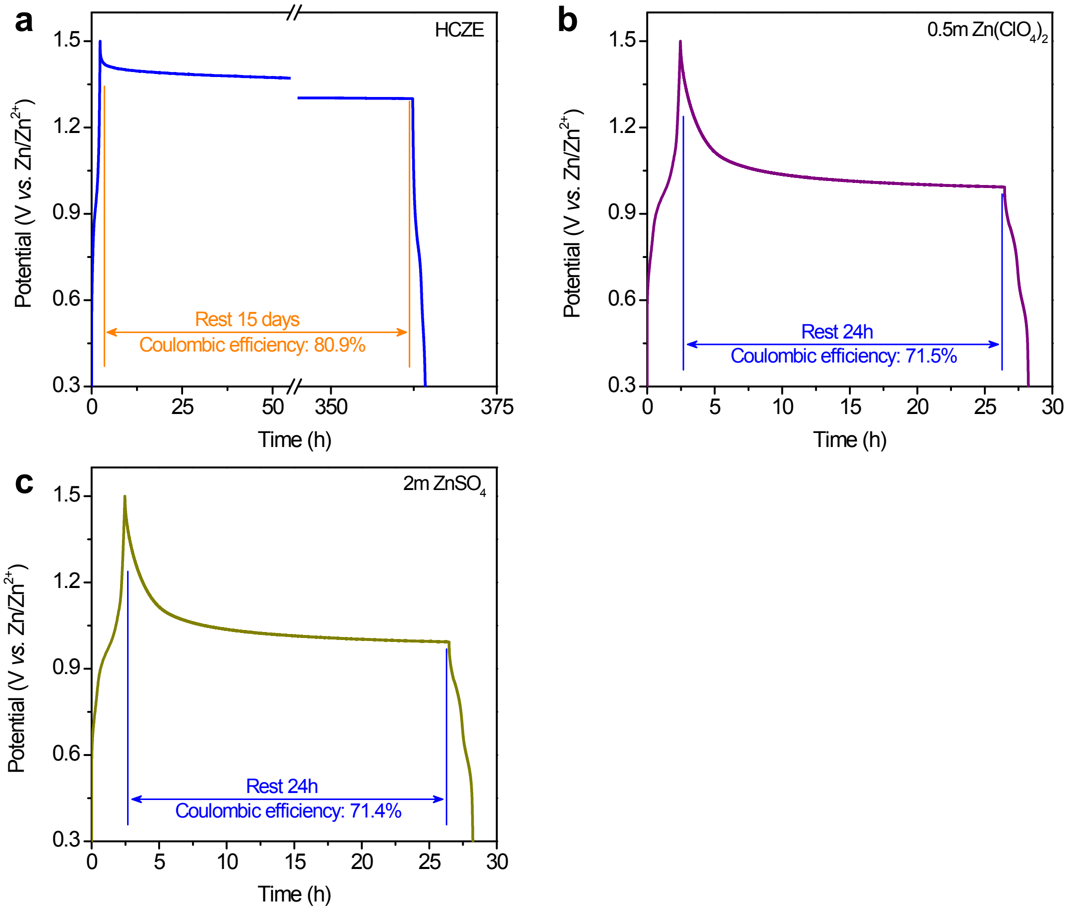

Fig. S29 Self-discharge performance of the NVO electrode in different electrolytes: (a) HCZE, (b) 0.5m $Zn(ClO_4)_2$, and (c) 2m $ZnSO_4$.

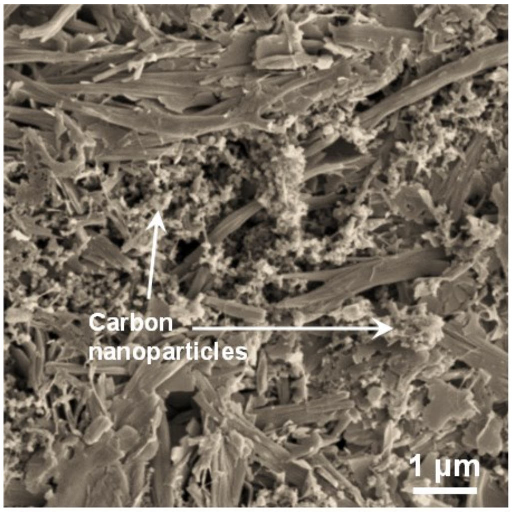

Fig. S30 SEM image of the NVO electrode at charged state after cycling stability test, showing the good maintenance of nanofibers.

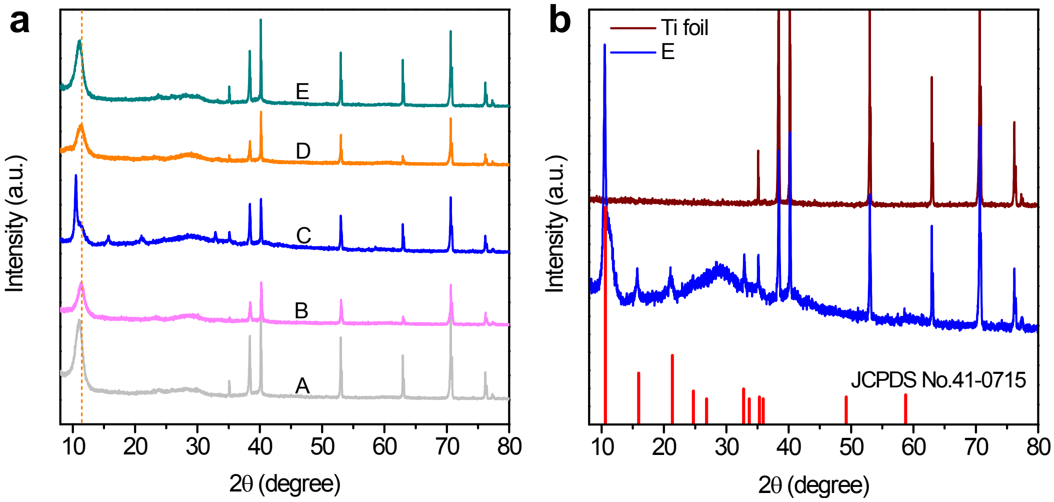

Fig. S31 *Ex-situ* XRD patterns of the NVO electrode in HCZE. States A-E represent the charge states labelled in Fig. 5d.

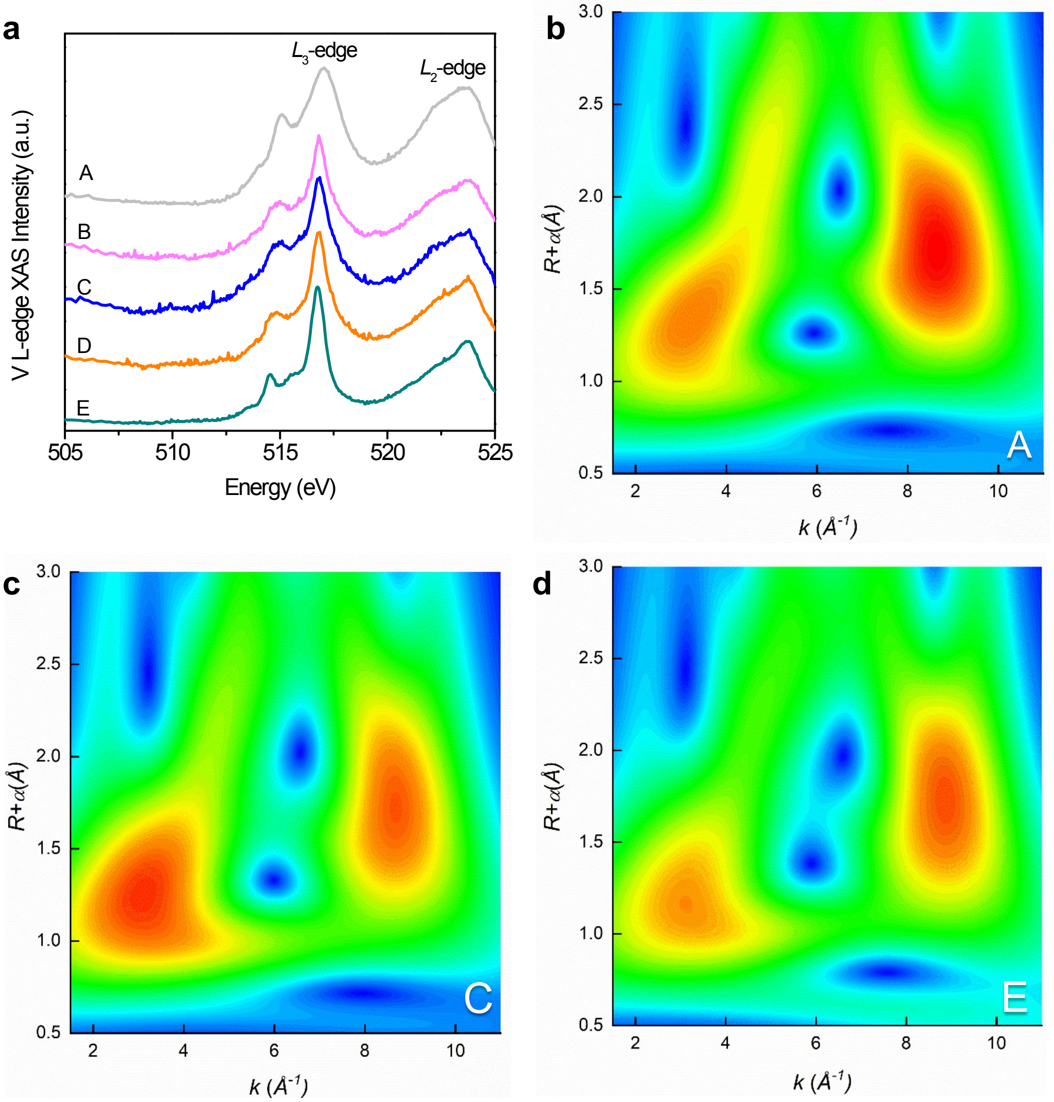

Fig. S32 *Ex-situ* X-ray absorption spectroscopy (XAS) of the NVO electrode in HCZE. (a) *Ex-situ* V $L_{2,3}$-edge soft XAS spectra of the NVO electrode in HCZE. (b-d) Wavelet-transformed XAS spectra of the NVO at selected states. As shown in Fig. S31a, the bulk-sensitive total fluorescence yield (TFY) spectra reveal that L_3-edge shows dramatic voltage-dependent changes, corresponding to the vanadium redox reactions in the bulk NVO. The L_2-edge exhibits broader features than the L_3-edge, which is due to the shorter lifetime of $2p_{1/2}$ core holes and the near-threshold Coster–Kronig decay.[S7] The wavelet representations show insignificant changes of V–O (3.2 $Å^{-1}$) and V–V (8.6 $Å^{-1}$), indicating the stable V_3O_8 bilayers of NVO to withstand Zn^{2+} and H^+ (de)intercalation.

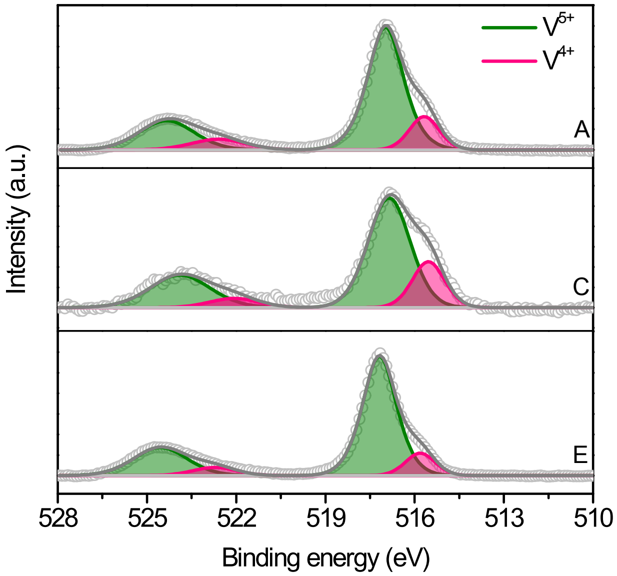

Fig. S33 *Ex-situ* V 2p core level of the NVO electrode in HCZE. The V^{4+} components intensify upon discharge (Zn^{2+} intercalation). This change is fully reversed when recharging to 1.5 V, wherein the V 2p core level is regenerated. The satellite peaks of V^{4+} states reveals a similar chemical environment to the pristine NVO electrode before the electrochemical reaction, highlighting the stable framework of V_3O_8 layers to withstand Zn^{2+} and H^+ (de)insertion.

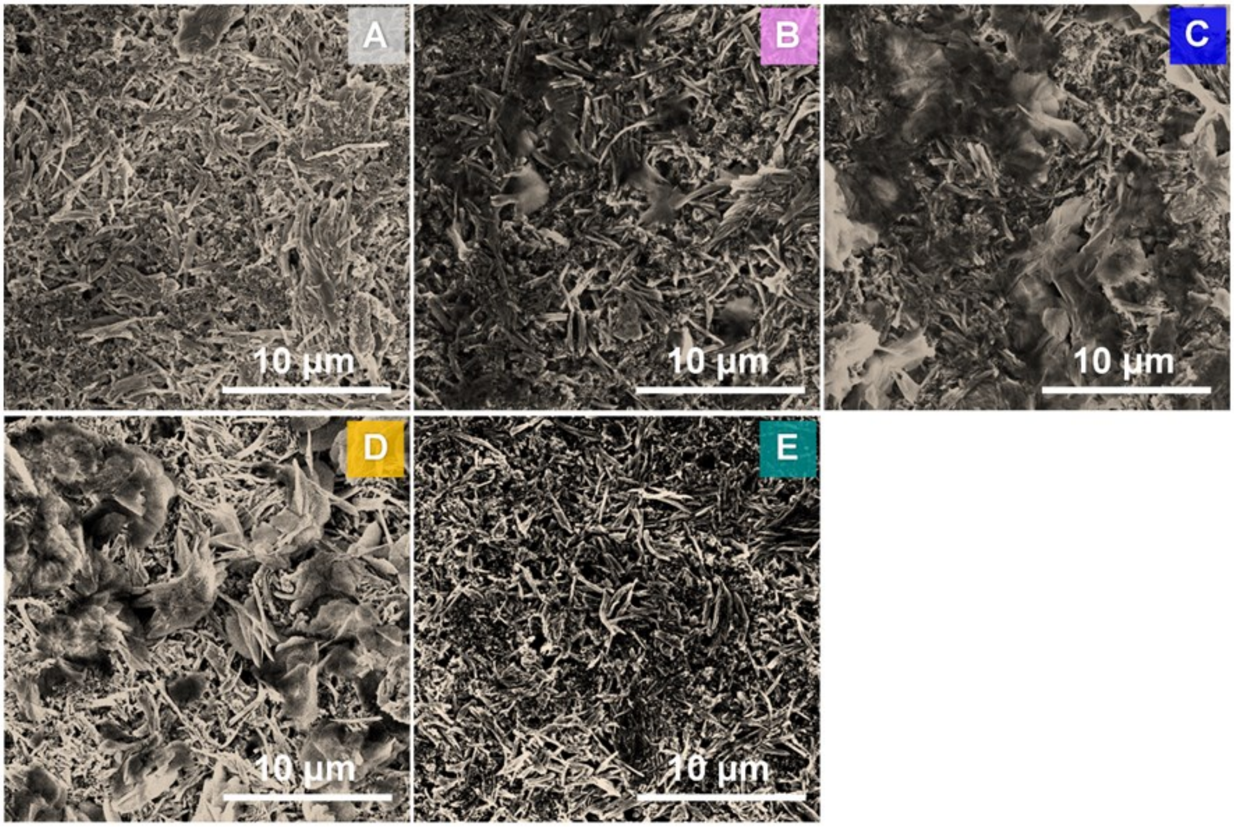

Fig. S34 *Ex-situ* SEM image of the NVO electrode in HCZE, showing the gradual generation of nanosheets on the electrode surface during discharge, which is followed by reversible disappearance of these nanosheets upon potential reversal.

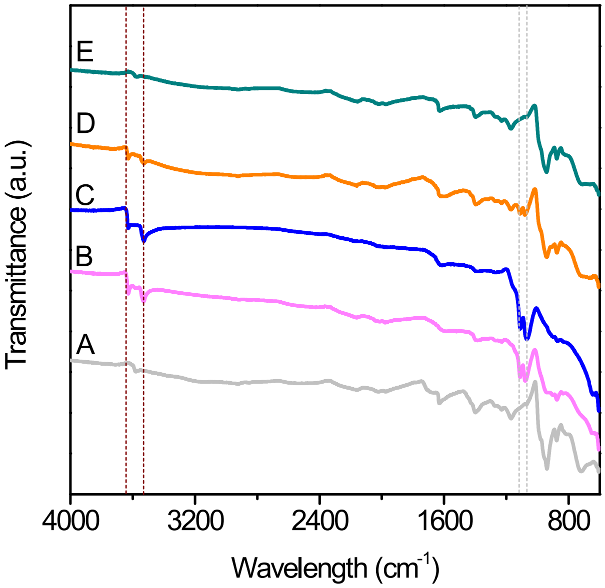

Fig. S35 *Ex-situ* ATR-FTIR spectra of the NVO electrode in HCZE. During discharge, typical V=O (945 and 880 cm^{-1}) and Na–O (1400 cm^{-1}) vibrations gradually decrease in intensity along with the appearance of new vibrations that can be attributed to ClO_4^- (1110 and 1075 cm^{-1}) and –OH (3630 and 3535 cm^{-1}).[S8,S9] These changes indicate the H^+ intercalations during the whole discharge process to generate $Zn_4ClO_4(OH)_7$, which could be deposited on the surface of NVO. The recharge process causes reversible changes of these vibrations, verifying the high reversibility of NVO in HCZE.

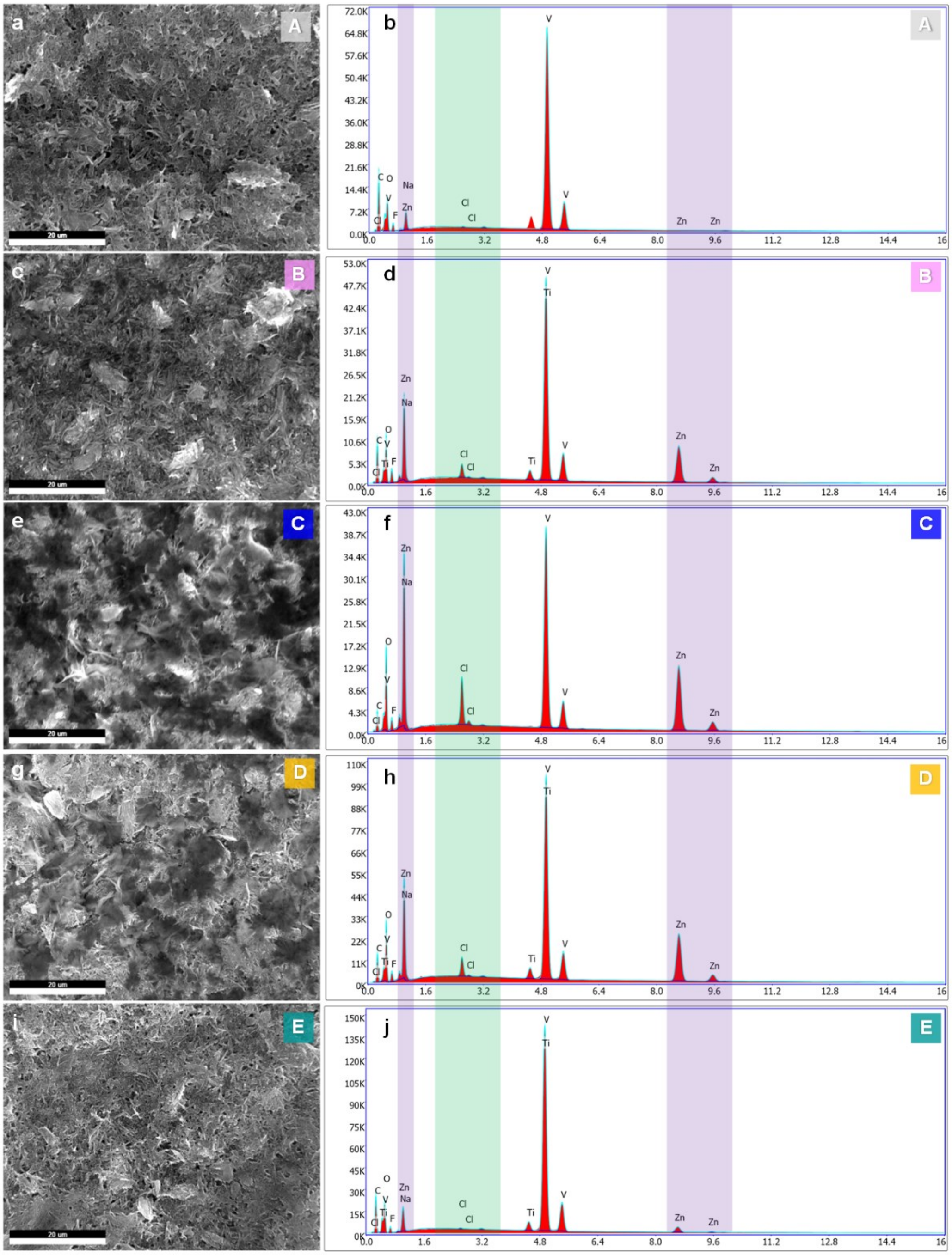

Fig. S36 *Ex-situ* SEM-EDS mapping and the corresponding EDS spectra of the NVO electrode in HCZE. The simultaneous changes of both Cl and Zn signals further confirm the simultaneous (de)intercalation of H^+ and Zn^{2+}.

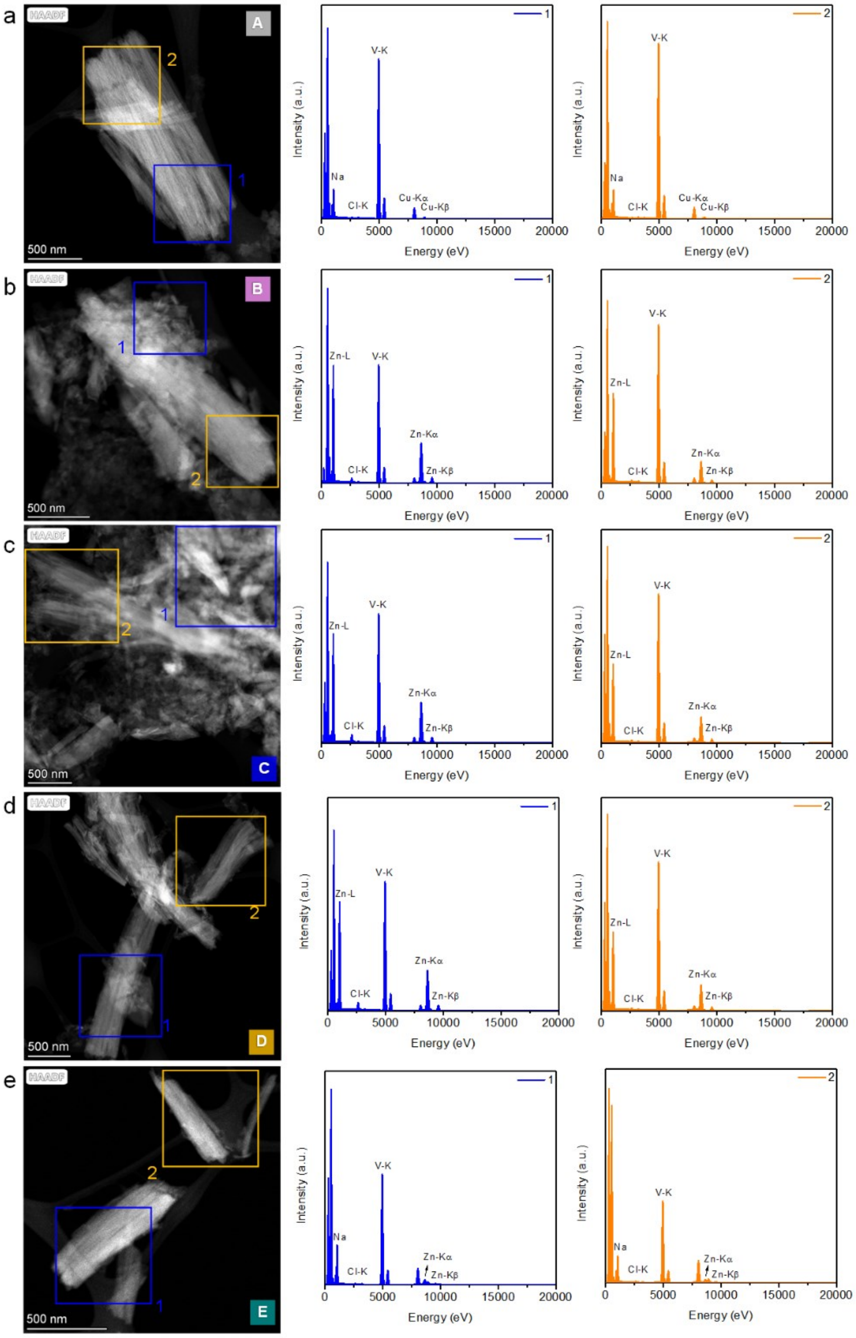

Fig. S37 *Ex-situ* TEM-EDS mapping and the corresponding EDS spectra of the NVO electrode in HCZE. Nanosheet-like products could be observed in the states of B, C, and D (Area 1), which is along with the strong Cl signals in the corresponding EDS spectra. This indicates the H^+ intercalation to form $Zn_4ClO_4(OH)_7$. In contrast, the absence of nanosheets and Cl signal in Area 2 reveal the reversible (de)intercalation into NVO. Through TEM-EDS, we confirmed the reversible and simultaneous H^+ and Zn^{2+} (de)intercalation within the NVO electrode at the nanoscale.

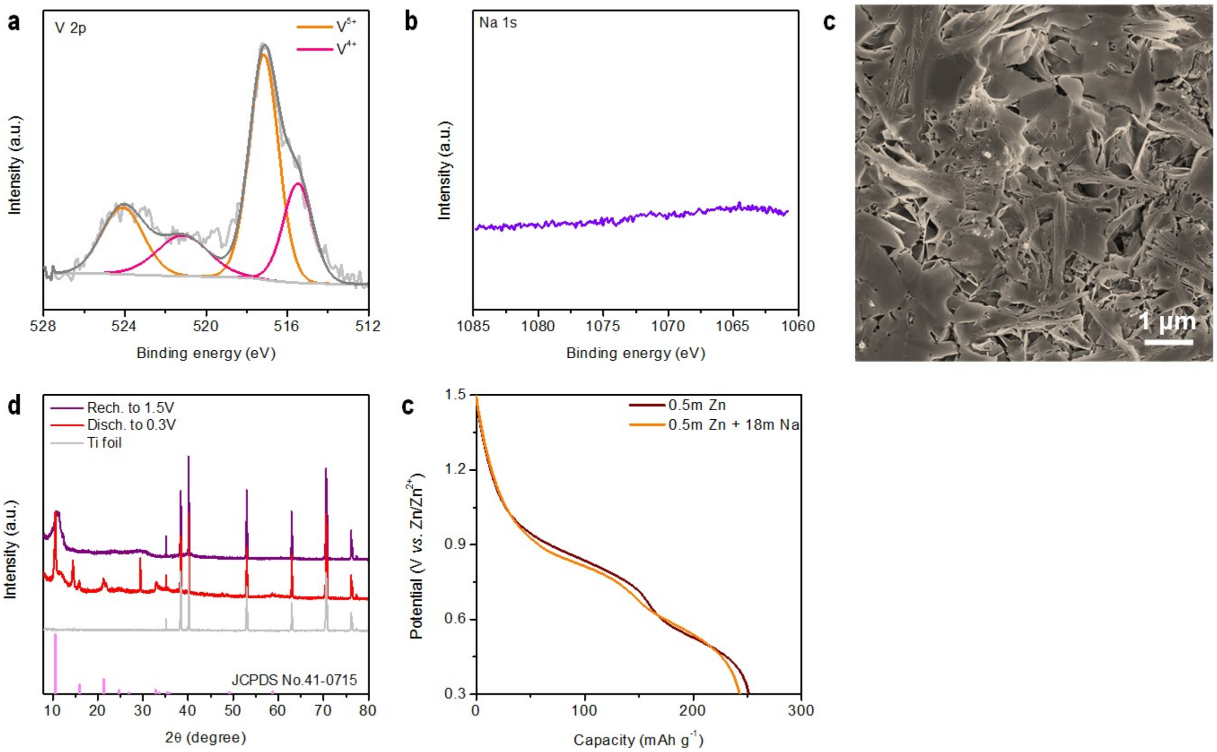

Fig. 38 (a) V 2p , (b) Na 1s core levels, (c) SEM image and (d) XRD patterns of the NVO electrode after discharging to 0.3 V in 0.5m $Zn(ClO_4)_2$. (e) Galvanostatic discharge plots of the NVO electrode in 0.5m $Zn(ClO_4)_2$ and HCZE at 0.1 A g^{-1}. The $Zn_4ClO_4(OH)_7$ nanosheets could be observed on the NVO electrode (Fig. S36c), indicating the successful H$^+$ cointercalation, as further confirmed by the XRD pattern (Fig. S36d).

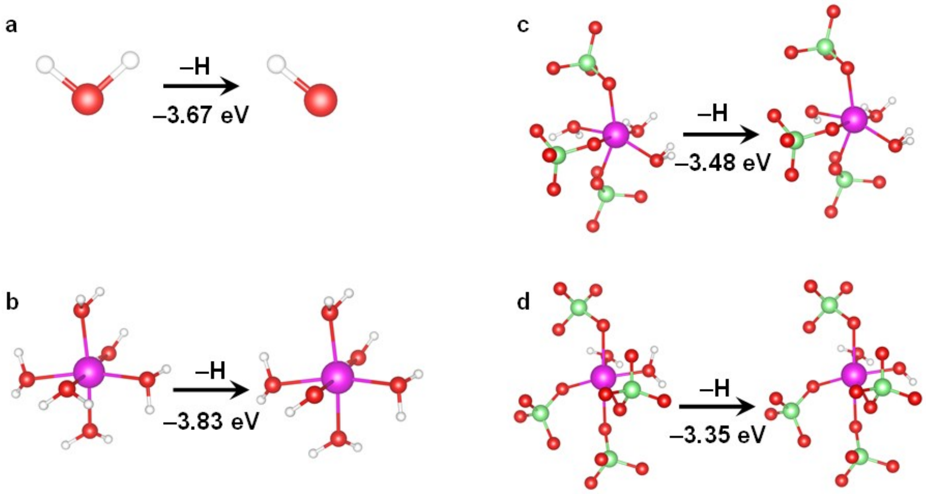

Fig. S39 Deprotonation energy calculated by DFT. (a) H_2O, (b) solvated Zn^{2+} in 0.5m $Zn(ClO_4)_2$, (c) solvated Zn^{2+} in 0.5m $Zn(ClO_4)_2$ + 9m $NaClO_4$, and (d) solvated Zn^{2+} in 0.5m $Zn(ClO_4)_2$ + 18m $NaClO_4$. Compared to the stable coordinated water molecules in the solvation sheaths of Zn^{2+} (Fig. S37c,d), the minimal amount of free water is more facile to deprotonation from the thermodynamics point of view (Fig. S37a). This reveals that the minimal amount of free water molecules could perform as the proton source during discharge.

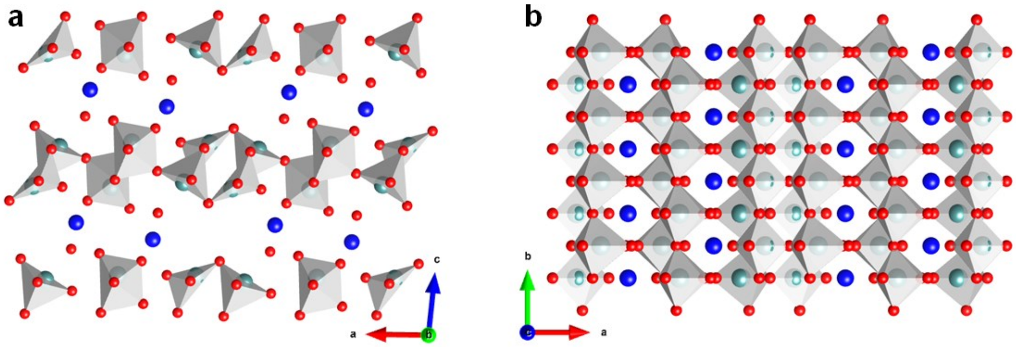

Fig. S40 Crystalline structure of the monoclinic NVO viewed along *b* axis (a) and *c* axis (b). Cyan ball: V, blue ball: Na, and red ball: O. The hydrogen atoms of water were not shown for simplicity.

3. Supplementary Tables.

Table S1. Summary of the atomic ratios of Zn and Cl of the NVO electrode in HCZE, determined by SEM-EDS and TEM-EDS.[a]

State	**SEM**		**TEM**			
			Area 1		**Area 2**	
	Zn (at%)	Cl (at%)	Zn (at%)	Cl (at%)	Zn (at%)	Cl (at%)
A	0	0.05	0.06	0.07	0.05	0.04
B	6.78	0.73	10.83	0.75	4.42	0.24
C	11.41	2.56	11.86	1.01	5.01	0.26
D	9.29	1.08	8.49	1.04	4.15	0.18
E	1.45	0.06	0.72	0.07	0.35	0.1

[a] The discharge product of $Zn_4ClO_4(OH)_7$ shows an atomic ratio of 4:1 for Zn/Cl. When the NVO electrode is discharge to 0.65 V and 0.3V and then recharged to 0.85 V, the Zn/Cl ratios for these three states are obviously higher than 4, confirming the Zn^{2+} intercalation besides H^+.

4. Supplementary Notes.

4.1. Supplementary Note 1.

Different vanadium oxides have been developed as promising cathodes with improved performance for reversible Zn^{2+} intercalation through regulating local electroneutrality and interlayer chemistry (*e.g.*, cation pillars, crystalline water).[S10] Typically, orthorhombic single-layer V_2O_5 is used as the precursor to prepare xerogel phase of bilayered vanadium oxide polymorph with expanded interlayer spacing to facilitate Zn^{2+} intercalation. This is because the limited interlayer spacing of 4.4 Å and high water solubility (8 g L^{-1} at 20 °C) make orthorhombic V_2O_5 unsuitable for aqueous ZIBs.[S11,S12] Recently, orthorhombic V_2O_5 has been proven to deliver high capacity and enhanced cyclability in concentrated $Zn(CF_3SO_3)_2$ electrolyte,[S12] though the long activation process (tens of cycles to reach maximum and stabilized capacity) make it difficult for practical application, especially when using lean electrolytes in practical batteries.[S13] Accordingly, using orthorhombic V_2O_5 to prepare its xerogel phases remains one of the research focuses in developing aqueous ZIBs. However, the conversion mechanism during the synthesis process has been scarcely studied.

To illustrate the formation mechanism of NVO nanofibers, we analyzed the reaction intermediates collected at different reaction stages. After mixing V_2O_5 powder with NaCl solution, we observed a gradual color change of the solid product from yellow to dark red. This is along with the color change of the solution from transparent to light yellow, suggesting the formation of VO_2^+ from the dissolution of V_2O_5.[S14] The XRD patterns of the reaction intermediates indicate the gradual disappearance of orthorhombic V_2O_5 phase, while the diffractions assigned to monoclinic NVO phase become more pronounced (Fig. S19). The morphological evolution of the solid intermediates can be revealed by SEM (Fig. S20). After reacting for 12 h, a small amount of nanofibers appeared and attached to the V_2O_5 nanoparticles. We believe that the V_2O_5 nanoparticles could perform as seeding sites for the heterogeneous nucleation of the nanofibers. Upon prolonging reaction time, the nanofibers kept growing in length, which finally reached several micrometers. The growth of nanofibers was along with the gradual disappearance of V_2O_5 nanoparticles, which is consistent with the XRD results (Fig. S21).

To better elucidate the formation details of NVO nanofibers, we conducted magic angle spinning nuclear magnetic resonance (MAS NMR) spectroscopy to analyze both the solid and liquid intermediates. Consistent with the XRD analysis, the ^{51}V NMR spectra of the solid reaction intermediates show the gradual disappearance of V_2O_5 phase (distorted VO_5 pyramid at –610 ppm) (Fig. S22a), which is accompanied with the appearance of two new signals at higher frequency (–654 and –670 ppm). These two new resonance peaks are assigned to monoclinic NVO phase, in which three non-equivalent V sites exist.[S15,S16] Two of these show octahedral symmetry while the third environment of V sites features a symmetry of distorted trigonal bipyramid. The resonance signal at –654 ppm corresponds to octahedral V sites. Since the increased quadrupole coupling effect of the second resonance peak at –670 ppm relates to a strong distortion of V sites, this peak is attributed to the V sites with more trigonal bipyramid environment. The broadening effect of these signals is due to a large distribution of each VO_x site, which is associated with slightly different V environment (*e.g.*, structural water, hydrogen bonding with V–O). The progressive formation of VO_x sites in monoclinic NVO is together with successful introduction of Na^+ into the structure of NVO, as confirmed by ^{23}Na NMR spectra of the solid intermediates (Fig. S22b). The quadrupole coupling and chemical shift anisotropy interactions are almost averaged at the testing spinning speed. The ^{23}Na NMR spectra show a broad signal at 2.8 ppm and a sharp signal at 14.1 ppm, which are attributable to the Na^+ sites that are close to and far away from water molecules, respectively.

Liquid-state ^{51}V MAS NMR studies indicate that the only solute species in the supernatant intermediates corresponding to cationic $[VO_2]^+$, which can perform as the reservoir of V^{5+} for NVO growth (Fig. S22c). The hydrolysis reactions of these two ionic species can be represented as:[S17]

$$[VO_2(H_2O)_4]^+ = [VO(OH)_3(H_2O)_2] + H^+ \tag{1}$$

The neutral $VO(OH)_3(H_2O)_2$ species could condense and then nucleate so fast that it could not be detected in the solutions. Of note is that this reaction (Equation 1) could decrease the pH of the solution. We found that the pH of the solution decreased with prolonging the reaction time, evidencing that this reaction prevailed during the synthesis process. On the other hand, the composition of V^{5+} in the solution can be changed with pH (Fig. S23), while the equilibrium of the cationic species in aqueous solutions follows the equations:[S18,S19]

$$[V(OH_2)_6]^{5+} + h H_2O = [V(OH)_h(OH_2)_{6-h}]^{(5-h)+} + h H_3O^+ \quad (2)$$

$$h = (0.244pH + 4.574)/(1 + 0.014pH) \quad (3)$$

wherein h denotes the hydrolysis ratio. Equation 2 is established on the partial charge model of octahedral V complex, which involves h and pH in the frame of the model.[S18] According to this relation, we may calculate that at a pH of 2.5 (supernatant intermediate collected after 12h reaction), the solution contains neutral $VO(OH)_3(OH_2)_2$ ($h = 5$). Furthermore, h decreases to 4.75 at pH = 1 (supernatant intermediate collected after 24h/48h/72h reaction). Accordingly, the supernatant solution should contain $[VO(OH)_{4.75}(OH_2)_{0.25}]^{0.25+}$. The rapid olation and oxolation reactions of these intermediates would lead to the formation of $[V_3O_8]^-$ layers, which could further condense with hydrated Na^+ to yield NVO nanofibers.[S14,S18] However, in the absence of NaCl, the V_2O_5 precursor nearly maintained the pristine crystalline structure and morphology after stirring in pure water for 3 days (Fig. S24). This indicates that the NaCl salt is an essential prerequisite for successfully synthesizing monolicnic NVO nanofibers. This could be strongly related to the increased chemical potential of the solution after introducing NaCl, which can accelerate the dissolution of V_2O_5 and the corresponding recrystallization to promote 1D nanostructure growth.[S20,S21] Noticeably, our dissolution-recrystallization strategy can be extended to synthesize cation-pillared vanadates with 1D nanostructures. Furthermore, we showcase the successful preparation of monoclinic $K_2V_6O_{16}\cdot nH_2O$ (space group: $P2_1/m$) nanofibers using the dissolution-recrystallization approach (Fig. S25), indicating the universality of our strategy to prepare unique cation-intercalation vanadate nanostructures with controllable morphology and properties.

4.2. Supplementary Note 2.

The CV curves of NVO shows slight shift of redox peaks as the scan rate increases, indicating the fast kinetics of our NVO electrode towards reversible Zn^{2+} storage (Fig. S26). This is associated with the ample interlayer spacing of NVO to accommodate Zn^{2+} intercalation and 1D nanostructure that can shorten solid-state diffusion length of Zn^{2+}. All the *ex-situ* characterizations clearly exhibit the reversible structural contraction/expansion and valence transition between V^{4+} and V^{5+} during Zn^{2+} and H^+ intercalation/deintercalation within NVO. As shown in Fig. S40, monoclinic NVO has layered (parallel to the (001) plane) and tunnel (perpendicular to the (001) plane) characteristics along the *b*- and *c*-axis, respectively. Nevertheless, the tunnel network is occupied by Na^+ ions, preventing the transportation of cations along the *c* axis. Therefore, the (001) plane along the *b* axis provides sufficient space for Zn^{2+} and H^+ migration across the layer of the gallery. The inserted cations can be accommodated in the pyramidal sites (O4–O4 in VO_5 is about 0.4 nm between the two V_3O_8 layers) between consecutive V_3O_8 layers since the Na^+ ions almost occupy the available octahedral sites and thus stabilize the overall framework. Accordingly, the intercalation of Zn^{2+} and H^+ clearly influences the XRD patterns as the (001) diffraction peak ($2\theta = 11.1^{\circ}$) gradually shifts to higher degree during discharge. Based on the aforementioned *ex-situ* measurements and elemental analysis, the electrochemical reactions of the Zn/NVO battery can be represented as:

Cathode: $5H_2O \leftrightarrow 5H^+ + 5OH^-$

$2.5Zn^{2+} + 0.36Zn(ClO_4)_2 + 5OH^- \leftrightarrow 0.72Zn_4ClO_4(OH)_7$

$Na_2V_6O_{16}\cdot nH_2O + 5H^+ + 0.6Zn^{2+} + 6e^- \leftrightarrow H_5Zn_{0.6}Na_2V_6O_{16}\cdot nH_2O$

Anode: $3.1Zn \leftrightarrow 3.1Zn^{2+} + 6e^-$

Overall: $Na_2V_6O_{16}\cdot nH_2O + 3.1Zn + 0.36Zn(ClO_4)_2 + 5H_2O$

$\leftrightarrow H_5Zn_{0.6}Na_2V_6O_{16}\cdot nH_2O + 0.72Zn_4ClO_4(OH)_7$

5. Supplementary References.

S1. G. Kresse, J. Hafner, *Phys. Rev. B*, 1993**, 48**, 13115−13118.

S2. G. Kresse, J. Furthmuller, *Phys. Rev. B*, 1996**, 54**, 11169−11186.

S3. Sodium perchlorate (Wikipedia). https://en.wikipedia.org/wiki/Sodium_perchlorate

S4. F. Wang, O. Borodin, T. Gao, X. Fan, W. Sun, F. Han, A. Faraone, J. A. Dura, K. Xu, C. Wang, *Nat. Mater.*, 2018, **17**, 543–549.

S5. F. Wan, Y. Zhang, L. Zhang, D. Liu, C. Wang, L. Song, Z. Niu, J. Chen, *Angew. Chem. Int. Ed.*, 2019, **58**, 7062–7067.

S6. P. Hu, M. Yan, T. Zhu, X. Wang, X. Wei, J. Li, L. Zhou, Z. Li, L. Chen, L. Mai, *ACS Appl. Mater. Interfaces*, 2017, **9**, 42717−42722.

S7. S.-M. Bak, R. Qiao, W. Yang, S. Lee, X. Yu, B. Anasori, H. Lee, Y. Gogotsi, X.-Q. Yang, *Adv. Energy Mater.*, 2017, **7**, 1700959.

S8. S. Cudziło, M. Nita, *J. Hazard. Mater.*, 2010, **177**, 146–149.

S9. F. Wan, L. Zhang, X. Dai, X. Wang, Z. Niu, J. Chen, *Nat. Commun.*, 2018, **9**, 1656.

S10. S. Liu, L. Kang, J. M. Kim, Y. T. Chun, J. Zhang, S. C. Jun, *Adv. Energy Mater.*, 2020, **10**, 2000477.

S11. J. L. Andrews, A. Mukherjee, H. D. Yoo, A. Parija, P. M. Marley, S. Fakra, D. Prendergast, J. Cabana, R. F. Klie, S. Banerjee, *Chem*, 2018, **4**, 564–585.

S12. N. Zhang, Y. Dong, M. Jia, X. Bian, Y. Wang, M. Qiu, J. Xu, Y. Liu, L. Jiao, F. Cheng, *ACS Energy Lett.*, 2018, **3**, 1366–1372.

S13. J. Liu, Z. Bao, Y. Cui, E. J. Dufek, J. B. Goodenough, P. Khalifah, Q. Li, B. Y. Liaw, P. Liu, A. Manthiram, Y. S. Meng, V. R. Subramanian, M. F. Toney, V. V. Viswanathan, M. S. Whittingham, J. Xiao, W. Xu, J. Yang, X.-Q. Yang, J.-G. Zhang, *Nat. Energy*, 2019, *4*, 180–186.

S14. J. Livage, *Chem. Mater.*, 1991, **3**, 578–593.

S15. J. Skibsted, N. C. Nielsen, H. Bildsoe, H. J. Jakobsen, *J. Am. Chem. Soc.*, **1993**, **115**, 7351–7362.

S16. M. Nadjafi, P. M. Abdala, R. Verel, D. Hosseini, O. V. Safonova, A. Fedorov, C. R. Müller, *ACS Catal.*, 2020, **10**, 2314−2321.

S17. J. Livage, *Coord. Chem. Rev.*, 1998, **178**, 999–1018.

S18. O. Durupthy, N. Steunou, T. Coradin, J. Maquet, C. Bonhomme, J. Livage, *J. Mater. Chem.*, 2005, **15**, 1090–1098.

S19. M. Henry, J. P. Jolivet, J. Livage, *Struct. Bonding (Berlin)*, 1992, **77**, 153–206.

S20. X. Rui, Y. Tang, O. I. Malyi, A. Gusak, Y. Zhang, Z. Niu, H. T. Tan, C. Persson, X. Chen, Z. Chen, Q. Yan, *Nano Energy*, 2016, **22**, 583–593.

S21. C.-J. Mao, H.-C. Pan, X.-C. Wu, J.-J. Zhu, H.-Y. Chen, *J. Phys. Chem. B*, 2006, **110**, 14709–14713.